Adaptive Link Optimization for 802.11 UAV Uplink Using A Reconfigurable Antenna

A Thesis

Submitted to the Faculty

of

Drexel University

by

Stephen Wolfe

in partial fulfillment of the

requirements for the degree

of

Master of Science in Electrical Engineering

June 2017

Dedications

To my family,

for their kind support

Acknowledgements

I would first like to thank Dr. Kapil Dandekar for his invaluable guidance and support over the past year. I also want to express my appreciation to Simon, Joe, and Danh who all provided much help and advice. I'd like to thank DWSL members for the experiences we shared.

Contents

List of Tables

List of Figures

List of Acronyms

AGL	Above Ground Level
AP	Adaptive Pursuit
ATC	Air Traffic Control
AWGN	Additive White Gaussian Noise
BEC	Battery Elimination Circuit
BPSK	Binary Phase Shift Keying
BLDC	Brushless Direct Current
CDF	Cumulative Density Function
CSI	Channel State Information
DFT	Discrete Fourier Transform
ESC	Electronic Speed Controller
EVM	Error Vector Magnitude
FAA	Federal Aviation Administration
FHSS	Frequency Hopping Spread Spectrum
GPS	Global Positioning System
GCC	GNU Compiler Collection
ICI	Intercarrier Interference
IID	Independent and Identically Distributed
IMU	Inertial Measurement Unit
LiPo	Lithium-ion Polymer
LTS	Long Training Symbol
LS	Least-Squares
LOS	Line Of Sight
MAB	Multi-Armed Bandit
MGTW	Maximum Gross Takeoff Weight
MCU	MicroController Unit
MLE	Maximum Likelyhood Estimate
MSL	Mean Sea Level

MAC	Medium Access Control
OFDM	Orthogonal Frequency Division Multiplexing
QAM	Quadrature Amplitude Modulation
NAS	National Airspace System
NLOS	Non-Line Of Sight
PC	Personal Computer
PDB	Power Distribution Board
PDF	Probability Density Function
PHY	Physical Layer
PMU	Power Management Unit
SDR	Software Defined Radio
SSE	Streaming SIMD Extensions
SIMD	Single Instruction Multiple Data
STS	Short Training Symbol
TWR	Thrust-to-Weight Ratio
RC	Remote Control
UAS	Unmanned Aerial System
UAV	Unmanned Aerial Vehicle
USRP	Universal Software Radio Peripheral
WLAN	Wireless Local Area Network

Abstract

Adaptive Link Optimization for 802.11 UAV Uplink Using A Reconfigurable Antenna

Stephen A. Wolfe

Advisor: Kapil R. Dandekar, Ph.D.

This thesis presents a low-cost and flexible experimental testbed for aerial communication research along with an implementation and experimental evaluation of an aerial-to-ground 802.11g link with an adaptive beamsteering antenna system. The system consists of a software-defined radio (SDR) platform, and a pattern reconfigurable antenna mounted on a hexacopter unmanned aerial vehicle (UAV). First, the system design aspects of the testbed are described. The performance of the reconfigurable antenna is characterized through radiation pattern measurements while the antenna is mounted on the underbelly of the UAV. A low complexity reinforcement learning based adaptive antenna selection algorithm is implemented on the aerial SDR testing platform to enhance the link quality. We present SNR measurements obtained during various indoor and outdoor flight scenarios. The results show that utilizing a reconfigurable antenna and intelligent antenna selection strategy onboard a UAV provides a higher mean SNR compared to an omni-directional antenna in both line of sight (LOS) and non-line of sight (NLOS) scenarios, and is more resilient to co-channel interference and reactive jamming.

1. Introduction

1.1 Motivation

Historically, UAV communications research has been primarily focused on medium to high-altitude fixed-wing UAVs on long endurance flights [6–9]. With the decrease in cost and increase in stability, multicopters have recently become very popular for commercial and consumer applications.

For many applications and environments, the mobility patterns of multicopters are desirable over fixed-wing UAVs. Unlike fixed-wing UAVs, multicopters possess the ability to land and takeoff vertically, and hover to hold a payload at a fixed aerial position. This makes multicopters easier to control and more suitable for situations where low-altitude flight is required, or when UAV movement is undesirable, especially in urban environments where aerial obstacles are present. Commercial Off-The-Shelf (COTS) drones, such as the DJI Phantom 4 [10], utilize WiFi links for video streaming and even UAV control. Multicopter based UAVs are currently being produced that are designed to carry surveillance systems and 4G base station payloads [11]. Also, Multicopter UAVs are being proposed as a solution for fast networking deployment in search-and-rescue and disaster relief scenarios [12].

Directional antennas on UAVs have been shown to increase the coverage of 802.11 systems [13] and increase system capacity [14]. However, the difficulty with using directional antennas on UAVs is that the antennas need to always be properly oriented, which is difficult to do in mobile environments such as UAV flight. Failure to maintain proper directional antenna orientation can result in

significant link degradation. As a result, most research utilizes omni-directional antennas on the UAV [9, 13, 15, 16].

Gu et al. [12] tackle the problem of adaptive antenna beamsteering for UAV-to-UAV IEEE 802.11 links by using a mechanical steering device onboard the UAV to keep the antenna pointed at the UAV. This approach is viable for aerial UAV-to-UAV links where line-of-sight (LOS) component are very likely to exist, however ground-to-UAV channels cannot assume LOS component exists and have more significant multipath scattering. Also, mechanical beamsteering devices are heavy and incur significant delays compared to electromagnetic beamsteering.

In this thesis, a system design for an aerial communication testbed is presented which consists of a low-cost UAV equipped with a compact SDR, and electrically reconfigurable directional antenna. The total weight of the platform is 2.2 kg, and maximum flight time of 15 minutes. The effect on the antenna radiation pattern due to near field scattering from the UAV body is characterized.

The onboard SDR is highly programmable and is capable of running GNU Radio, which is a popular open-source SDR development platform [17]. There are many open-source GNU Radio projects for various purposes such as wireless channel characterization, spectrum monitoring, and communication links. The onboard radio system is capable of running these projects in an aerial environment.

Furthermore, the aerial SDR platform is used to address the issue of adaptive antenna beamsteering on UAVs by using an electrically reconfigurable directional antenna combined with reinforcement learning based antenna beam selection algorithm for 802.11 links. The general strategy of the adaptive beamsteering algorithm was introduced by [18, 19]. The algorithm is tuned with the data obtained

from the SNR characterization flights, and we compare the performance of the algorithm to an omni-directional antenna under various scenarios (Figure 1.1).

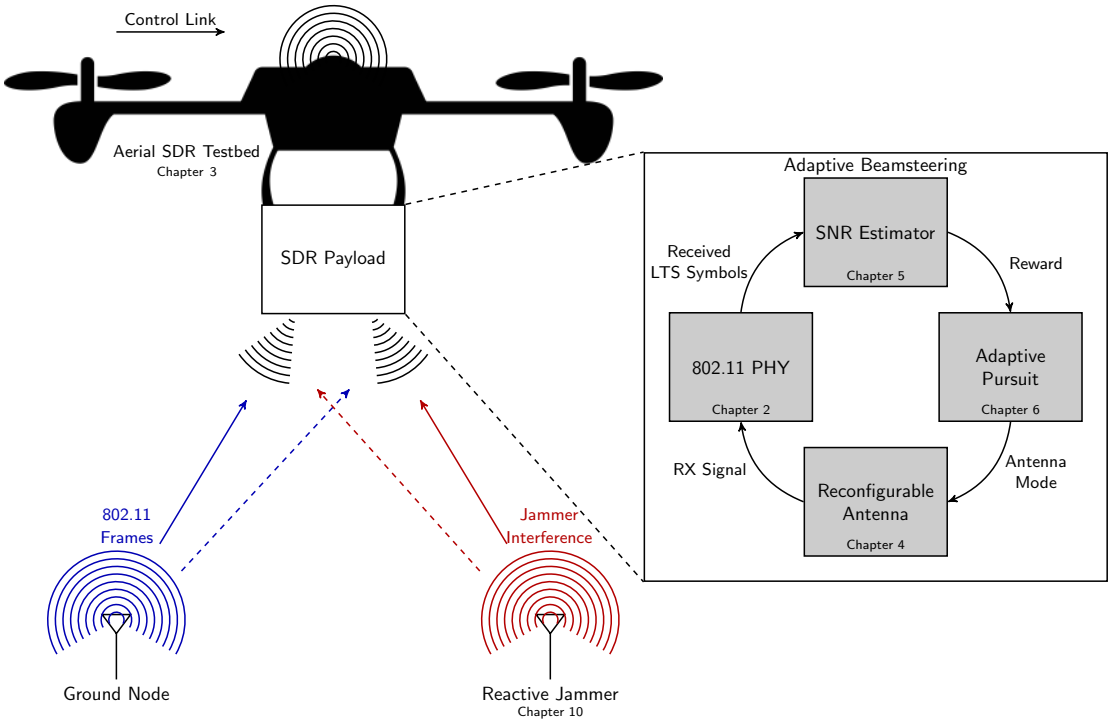

FIGURE 1.1: Aerial SDR system and adaptive beamsteering concept diagram

1.2 Contributions

The idea of adaptive beamsteering has been proposed and analyzed in simulation for fixed-wing UAVs [20], however there is a lack of experimental results. There is even less literature regarding adaptive beamsteering methods geared toward multicopter UAVs. In this thesis, we take a reinforcement learning algorithm called adaptive pursuit [21] which has been previously used for terrestrial beamsteering [19] and evaluate its performance in UAV-to-ground channels. To the

best of our knowledge, this work in this thesis presents the first experimental results that utilize electrically reconfigurable antennas and adaptive beamsteering in multicopter-to-ground wireless links to optimize link quality and avoid adversarial reactive jammers.

All previous multicopter-based wireless experimentation has been performed with inflexible components such as very basic transmitters and COTS access points [9, 12, 13, 15, 16], The system design for the aerial SDR platform is the first multicopter-based aerial SDR platform that is highly reprogrammable.

The SDR software configuration to implement 802.11-based adaptive beamsteering involved enabling ARM support on the gr-ieee-80211 GNU Radio project, which was previously only compatible with x86-based devices, so it can be used on a Raspberry Pi 3 [22]. The relevant changes were accepted by the project maintainer [23] so that future users can use the project on ARM devices.

A conference paper that describes the system design of the aerial SDR testbed and adaptive beamsteering algorithm is currently under review [24]. An IEEE transactions letter is in progress which describes anti-reactive jamming related experiments and results.

2. Background

Most modern COTS multicopter UAVs communication links are 802.11-based. Some commercial multicopter systems may contain proprietary encoder modifications [25], and open source projects seek to modify the Medium Access Control (MAC) layer to support unidirectional broadcasts for low-latency UAV video streaming. The 802.11 physical layer remains mostly unchanged.

There are several reasons why 802.11 is prevalent in COTS multicopter links. The most significant reason is consumer demand for live video streaming and control from common electronic devices such as smart phones and tablets, which generally have 802.11 capabilities. 802.11 also offers good performance in mobile links. It has been shown that Orthogonal Frequency Division Multiplexing (OFDM)-based 802.11 links provide good performance in high-speed UAV wireless channels, which have larger Doppler shift and Inter-Carrier Interference (ICI) [26]. Multicopter UAVs are typically used for low-speed low-altitude flights, which better facilitates 802.11 links than high-speed fixed-wing UAVs.

A significant portion of the work presented in this thesis focuses on adaptive optimization the quality of wireless IEEE 802.11 links utilizing physical layer characteristics. This chapter presents the background theory behind this thesis work, which includes channel modeling and the basic structure of the 802.11 physical layer.

2.1 OFDM Basics

OFDM is the 802.11 modulation format. OFDM utilizes multiple QAM subcarriers in a manner that is both spectrally efficient and minimizes ICI. These

characteristics are achieved by spacing subcarriers such that the spectral peak of a given subcarrier is at a null for all other subcarriers, which is possible because each subcarrier has a sinc shaped frequency profile (Figure 2.1). The subcarriers should be spaced at $\frac{1}{T_d}$ Hz intervals, where T_d is the symbol duration. 802.11 symbols have a length of 4 μs, which includes a guard interval of 0.8 μs, so the symbol duration is 3.2 μs. The subcarrier spacing of 312.5 KHz can therefore be calculated as follows:

$$\Delta f = \frac{1}{T_d} = \frac{1}{3.2\,\mu\text{s}} = 312.5\,\text{KHz} \tag{2.1}$$

The OFDM symbol is based on a 64-point DFT, which leads to a total bandwidth of $64\,(312.5\,\text{KHz}) = 20\,\text{MHz}$.

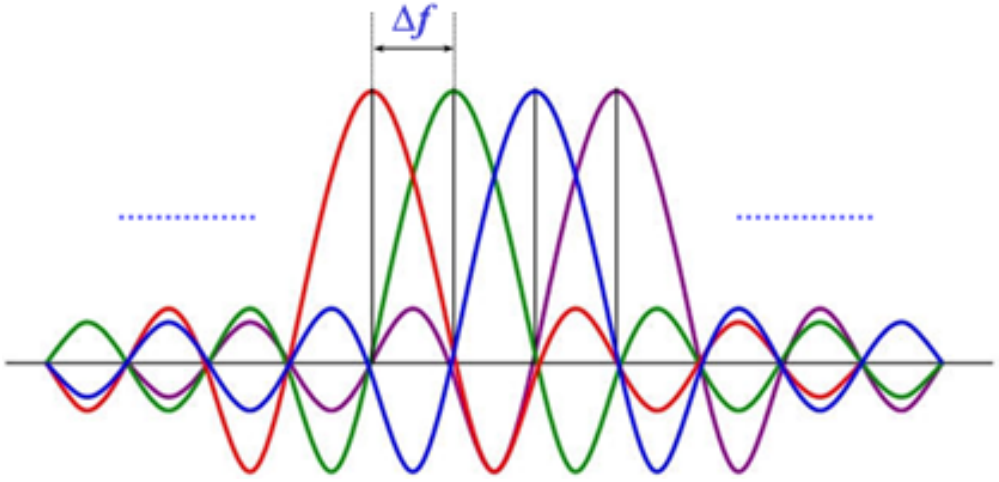

FIGURE 2.1: ODFM subcarrier layout[1]

For each symbol, the receiver downconverts the received I/Q channels to baseband to form the extracted complex time-domain signal $y_s[n]$. The receiver

computes the N-point Discrete Fourier Transform (DFT), to determine the received constellation point, $Y_s(k)$ at each subcarrier[1] (Equation 2.2).

$$Y_s(k) = \sum_{n=0}^{N-1} y_s[n]\, e^{-\frac{2\pi j}{N} kn} \tag{2.2}$$

The received symbol is then equalized via a process explained in Chapter 5, and the transmitted symbol is estimated.

2.2 Channel Model

Each ODFM subcarrier is modelled individually as a flat-fading channel. At each subcarrier, the receiver recovers a constellation point Y, which is a rotated and scaled (typically attenuated) version of the transmitted constellation point X caused by channel effects, plus Additive White Gaussian Noise (AWGN) caused by various noise sources, such as electrical noise on the receiver's RF frontend, co-channel interference, and ICI due to the increased Doppler effects caused by the mobile channel conditions. The received constellation point on symbol s at subcarrier k can be therefore be modeled as:

$$Y_s\,(k) = H\,(k)\, X_s\,(k) + W(k) \tag{2.3}$$

Where $X_k\,[n]$ and $Y_k\,[n]$ are the transmitted and received complex symbols for subcarrier i, respectively. $W(k)$ is AWGN with subcarrier noise power $N(k)$ (i.e. $W(k) \sim \mathcal{N}_c\,(0, N_k)\,$). H is the Channel State Information (CSI) which is a complex number describing channel's scaling and rotation of the received symbol.

[1]The work on this thesis focuses on the receiving end of an 802.11 link. The OFDM modulation, which basically is the inverse of the demodulator, is not explained in this thesis.

It is assumed that the OFDM frame duration is less than the channel coherence time, therefore $H(k)$ is treated as a constant throughout the duration of a frame. The amplitude of CSI is proportional to the amplitude of the received signal, Therefore, $|H(k)| = \sqrt{P_{RX}(k)}$, where $P_{RX}(k)$ is the received subcarrier signal power.

2.3 Channel Fading

Due to various channel factors such as multipath propagation and movement, the channel characteristics are time-varying. CSI and therefore received signal power is not constant and are constantly fluctuating. The effects of channel fading can be modeled by treating the magnitude[2] of the observed CSI at each frame an Independent and Identically Distributed (IID) random variables. The distribution of CSI is dependent on assumptions about the channel, particularly the prominence of a Line-of-Sight (LOS) component of the received signal.

In high multipath conditions where no dominant LOS path exists, it is assumed that CSI has real and complex components distributed as IID Gaussian distribution with zero mean and a variance σ^2. Therefore, $H = X + jY$, where $X, Y \sim \mathcal{N}(0, \sigma^2)$. The CSI amplitude $|H|$ can then be calculated via $\sqrt{X^2 + Y^2}$, which implies $|H| \sim \text{Rayleigh}(\sigma)$. Where a Rayleigh distribution is defined via the following Probability Density Function (PDF):

$$X \sim \text{Rayleigh}(\sigma) \implies f_X(x) = \frac{x}{\sigma^2} e^{-\frac{x^2}{2\sigma^2}}$$

and the total received signal power is $P_{RX} = 2\sigma^2$

[2]CSI phase is also fluctuating, however phase has no effect on received signal strength, therefore it is not analyzed in the context of fading

In UAV air-to-ground, it is not uncommon for there to also be a LOS signal component [27, 28]. When a LOS path is present, the received signal consists of both LOS and multipath components. The multipath component of the received signal is modeled in a similar manner as in the Rayleigh distribution, and the LOS portion shifts the mean of the H. CSI in a fading channel with multipath power $2\sigma^2$ and LOS power ν^2 is can be modeled as $H = X + jY$, where $X \sim \mathcal{N}(\nu\cos\theta, \sigma^2)$ and $Y \sim \mathcal{N}(\nu\sin\theta, \sigma^2)$. This implies that $|H| \sim \text{Rician}(\nu, \sigma)$. A Rician distribution has the following PDF:

$$f(x) = \frac{2(K+1)x}{P_{RX}} \exp\left(-K - \frac{(K+1)x^2}{P_{RX}}\right) I_o\left(2\sqrt{\frac{K(K+1)}{P_{RX}}}x\right) \tag{2.4}$$

Where I_o is the 0^{th} order modified Bessel function of the first kind. P_{RX} is the scale parameter which is the total power from both LOS and multipath components ($P_{RX} = \nu^2 + 2\sigma^2$). K is the shape parameter, which is the ratio between the LOS power (ν^2) and scattered multipath power ($2\sigma^2$)

$$K = \frac{\nu^2}{2\sigma^2} \tag{2.5}$$

2.3.1 UAV air-to-ground Channels

Preliminary air-to-ground channel measurements have been presented in [27], however these measurements were taken in military fixed-wing aircrafts at unspecified altitudes and velocities[3]. The measured Rician K-factor varied from 5 to 250.

[3]It is safe to assume the fixed-wing aircraft was still at a much higher speed and altitude than the UAV experiments conducted in this thesis.

The experiments conducted in this thesis is at a lower altitude in urban environments which likely has much more significant scattering than observed from high altitude fixed-wing aircrafts. Therefore, it is safe to assume the Rician K-factor will be lower than the measurements provided by [27]. This assumption agrees with measurements provided in [28] which shows that lower elevation angles[4] leads to lower Rician K-factors.

2.4 802.11 OFDM Frame Structure

IEEE 802.11 is a set of Physical Layer (PHY) and Media Access Control (MAC) specifications for a Wireless Local Area Network (WLAN) [29]. Many IEEE 802.11 standards exist, and the most recent standards are nearly all based on OFDM modulation format. While the experimental work in this thesis utilizes 802.11g, the adaptive link optimization technique utilizes portions of the frame that is present in most OFDM-based 802.11 standards including 802.11a/g/p.

IEEE 802.11 frames begin with a preamble that consists of two types of training sequences: a Short Training Sequence (STS), followed by a Long Training Sequence (LTS) (Figure 2.2). The STS is used for frame detection, AGC and coarse frequency offset estimation, while the LTS is used for channel estimation and fine frequency offset estimation. This chapter focuses on how the receiver acquires channel estimates from the LTS training sequence using a least-squares (LS) channel estimation approach.

IEEE 802.11 frames consist of 64 subcarriers across 20 MHz. There are 48 subcarriers, and 4 pilot subcarriers, and 12 null subcarriers. Therefore, only 52 subcarriers are utilized (Figure 2.3). Each subcarrier uses Quadrature Amplitude

[4]The angle above the horizon between the UAV and ground node

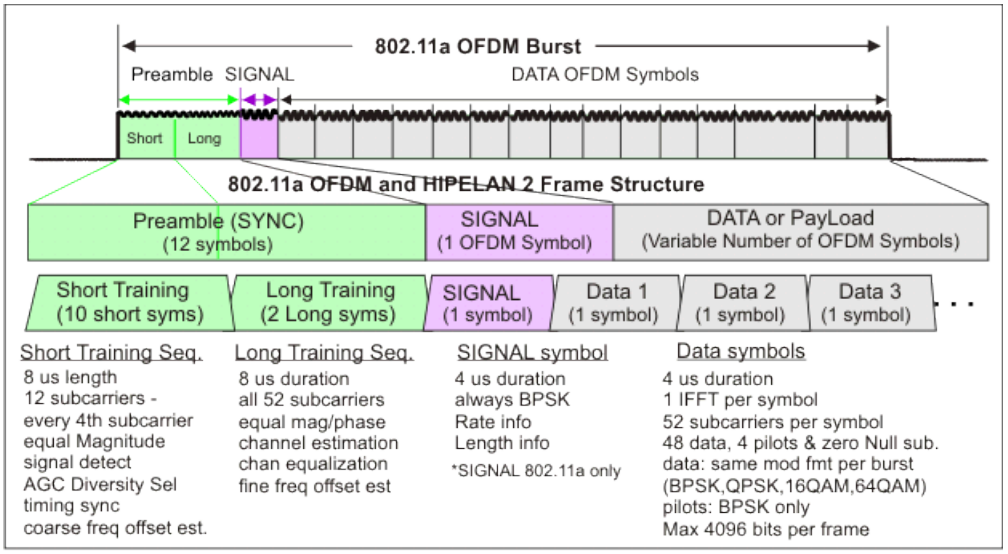

FIGURE 2.2: Temporal IEEE 802.11 OFDM frame structure [2]

Modulation (QAM) of bit-rates ranging from Binary Phase Shift Keying (BPSK) to 64-QAM.

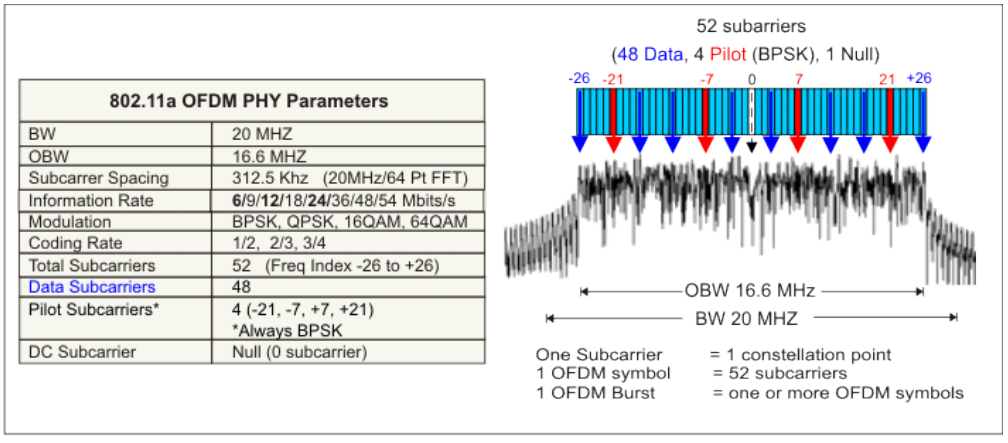

FIGURE 2.3: Spectral IEEE 802.11 ODFM frame structure [2]

3. System Design

The aerial SDR system consists of a multicopter UAV, hosting a radio system payload. The radio system payload of a SDR, host computer, and reconfigurable antenna (Figure 3.1). Other than the reconfigurable directional antenna, the aerial SDR system is made entirely of affordable COTS components. The UAV system weight is 1.9 kg, and radio payload weighs 0.3 kg, which produces a gross system weight of 2.2 kg. The aerial SDR system is capable of 15-minute flight time and has a 2.1 thrust-to-weight ratio.

FIGURE 3.1: Aerial SDR System

3.1 UAV

The aerial SDR system was based around the DJI F550 hexacopter airframe [10] which provides additional assembly space, stability, and payload capacity compared to quadcopter airframes (Table 3.1), but is cheaper and more suitable for indoor testing than an octocopter. However, increasing the number of rotors from

TABLE 3.1: Multicopter decision matrix

Attribute	Quadcopter	Hexacopter	Octocopter
Efficiency / Flight Time	High	Medium	Low
Maneuverablility	High	Medium	Low
Indoor Suitability	High	Medium	Low
Stability	Low	Medium	High
Payload Capacity (Weight)	Low	Medium	High
Assembly Space	Low	Medium	High
Cost	Low	Medium	High
Redundancy	Low	Medium	High

four to six does lead to reduced power efficiency. The F550 airframe is commonly used for prototyping, and has been previously utilized for aerial communication experimentation [12].

The entire aerial SDR system is powered by a 4S 5500 mAh 35C LiPo battery. The battery has a nominal voltage of 14.8 V and weighs 538 g. A step-down converter and regulator were used to create an onboard a 5 V DC power source, which is used to power the SDR system and antenna. The battery terminals (V_{batt} and GND), are connected to the power distribution board (PDB) on the F550 airframe (Figure 3.2). The PDB routes battery power to the base of all rotor arms, to power ESCs and motors, and to the center of the airframe to power the flight control system and SDR payload (Figure 3.2). Both flight control system and SDR payload system require DC at a specific voltage. A Power Management Unit (PMU) module is used to regulate power supplied to the flight control system. A DC/DC converter is used to regulate power supplied to the SDR payload system.

Power efficiency is important for battery powered aircrafts. UAVs that have poor power efficiency suffer from shorter flight times. Over 95% of the battery

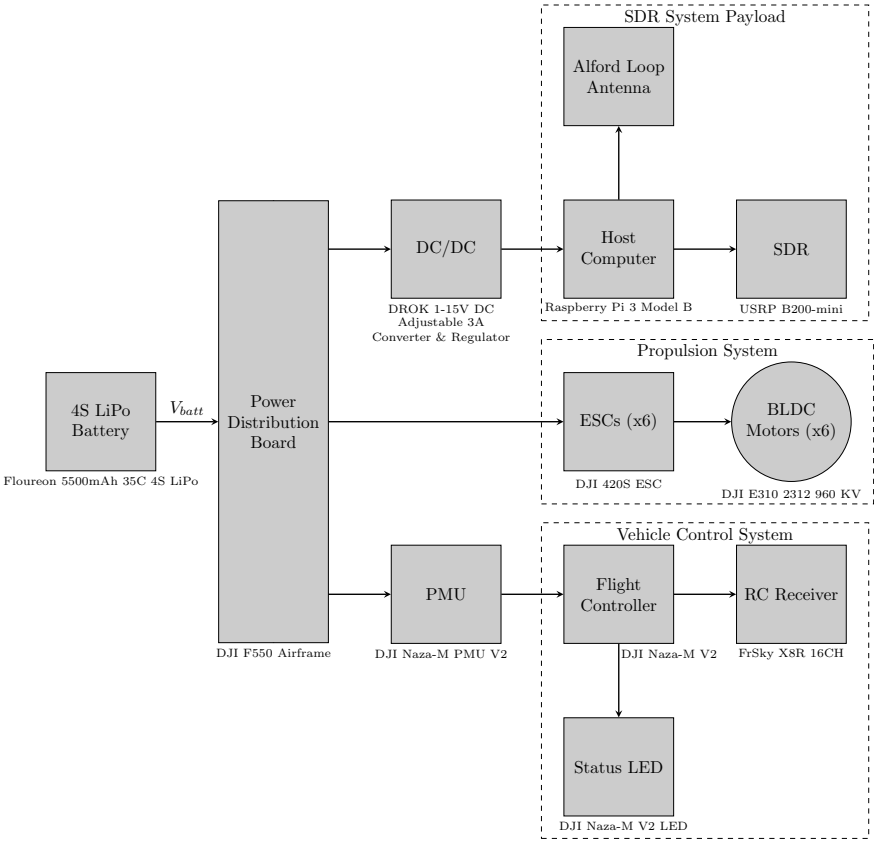

FIGURE 3.2: Onboard system power flow diagram. Antenna is described in [3]

power is consumed by the UAV's propulsion system, which consists of Brushless DC (BLDC) motors, propellers, and electronic speed controllers[1] (ESC). Therefore, a power efficient propulsion system will significantly increase the UAVs maximum flight time. The propulsion system components should be selected based on interoperability and suitability for the aircraft's weight and dimensions, and battery voltage. The aerial SDR system uses the DJI E310 Tuned Propulsion System which is designed to be suitable for F550 airframe [10]. The E310 system consists of 960 kV brushless motors, 9.4 in diameter propellers with a pitch of 5 in, and ESCs rated for 20 A continuous current. The maximum thrust (F_T) of the E310

[1]BLDC motors do not have an internal mechanical commutator, and therefore require the ESCs to perform commutations. The ESC drives the motors by controlling current through the motor coils via three phase leads connected in a wye configuration.

propulsion system is 800 g/rotor, which totals 4.8 kg of thrust. This produces a thrust-to-weight ratio of approximately 2.1, providing enough control authority for the system to be capable of handling moderate wind conditions.

The DJI Naza-M V2 flight controller is used to stabilize and control the UAV [10]. The flight controller detects its attitude and altitude via onboard sensors 3-axis gyroscope and a 3-axis accelerometer, and barometer, and then controls the speed of each motor to maintain stability. The flight controller also supports GPS assisted flight, however the GPS was not used as most testing was performed indoors. The flight controller responds to movement commands sent by the remote pilot using a FrSky Taranis transmitter, which sends UAV movement commands to a FrSky X8R receiver onboard the vehicle over a 2.4 GHz FHSS control link. The X8R receiver recovers the control commands and sends them directly to the flight controller (Figure 3.4).

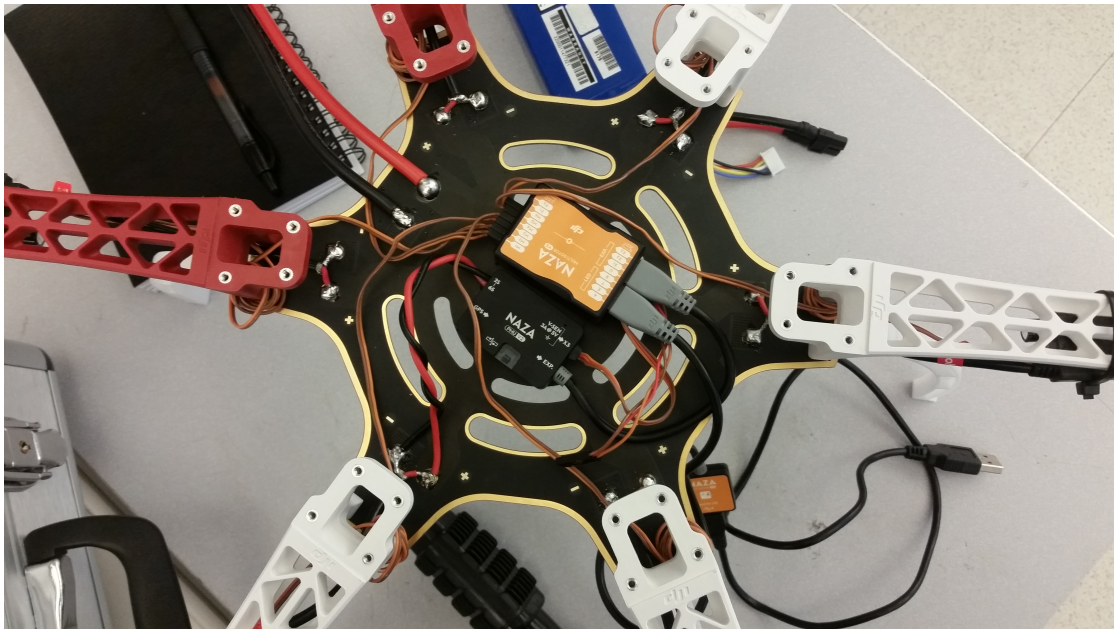

FIGURE 3.3: Naza V2 flight controller mounted in the center of the vehicle next to the PMU. (The SDR payload was not mounted on the vehicle in this photograph.)

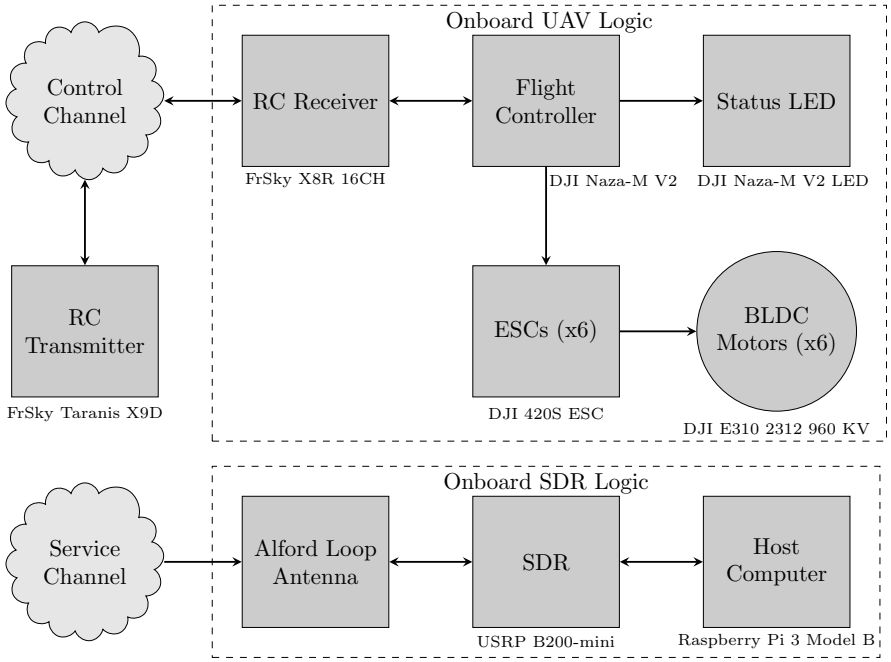

FIGURE 3.4: System logic flow diagram. The UAV system and radio payload are logically isolated. Antenna is described in [3].

3.2 SDR

The SDR system consists of lightweight, small form factor components, which are ideal for UAV applications due to weight and mounting space constraints. The selected components are as lightweight as possible while still providing reasonable performance. The onboard radio system consists of a USRP B200mini, which is a credit-card sized PCB weighing only 24 g [30]. A Raspberry Pi 3 Model B, which is a small single-board computer weighing 42 g. with an quad-core ARM Cortex-A53, was used to serve as a host to the B200mini. The B200mini and Raspberry Pi 3 communicate over a USB 2.0 interface. The SDR system is logically isolated from the UAV flight control system logic. No information about the UAV state is passed to the radio payload, and vice versa.

The adaptive beam-steering implementation work was based off the framework of a GNU Radio recipe containing a IEEE 802.11a/g/p SDR transceiver

design [22]. Only the physical layer of this transceiver was utilized, which was modified to enable reconfigurable antenna state control and implement the adaptive beamsteering algorithm. The physical layer of this transceiver was modified to enable reconfigurable antenna control and the adaptive beamsteering algorithm explained in Chapter 6.

3.2.1 Enabling ARM support in gr-ieee-80211

GNU Radio does support ARM platforms [31] such as the Raspberry Pi 3, but it is primarily used on x86 platforms. While generic GNU Radio offers support for ARM platforms, not all GNU Radio recipes support ARM architecture. The gr-ieee-80211 recipe only supported x86, and had never been previously used on any ARM-based platform.

The primary reason for the lack of support for ARM platforms were unconditional calls to x86 intrinsic instructions in the punctured Viterbi decoder implementation. The existing Viterbi decoder utilized Streaming SIMD (Single Instruction Multiple Data) Extensions (SSE2) to increase performance. SIMD instructions are processor instructions that operates on multiple data elements per instruction in a vector-like manner [32]. SSE2 is an SIMD instruction set specific to x86 architecture. Non-x86 architectures are not able to utilize SSE2 instruction set, but typically offer SIMD instruction sets similar to SSE2. The solution was to write an additional generic punctured Viterbi decoder implementation that does not use SIMD instructions. The implemented generic punctured Viterbi decoder was heavily based off of the Viterbi decoder in a different GNU Radio recipe for digital TV broadcasting called gr-dtv which is also OFDM-based and utilizes a similar decoder [33]. This new generic Viterbi decoder was added alongside the SSE2 implementation. The proper Viterbi decoder is selected based on compiler

flags which denote the supported SIMD instruction sets at compile time (Figure 3.5).

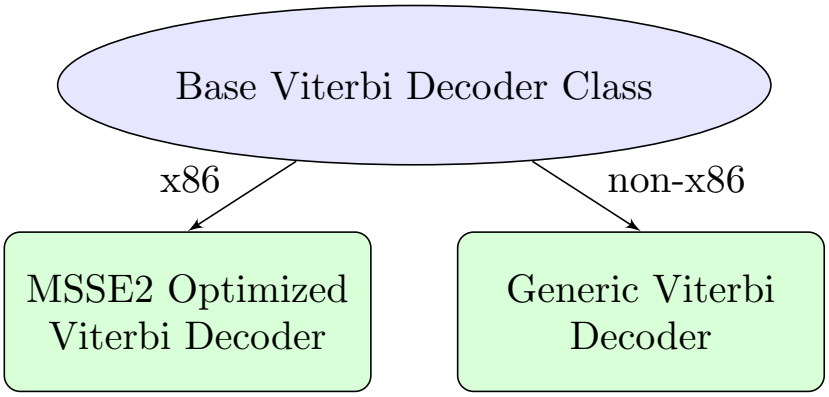

FIGURE 3.5: Viterbi Decoder Structure

The Viterbi decoder changes that provide cross-platform support are valuable to the GNU Radio community as they allow anyone to use the 802.11 recipe on an ARM device. The changes were presented to the gr-ieee-80211 author and maintainer, who decided to merge the changes to the upstream gr-ieee-80211 repository [23].

3.3 Aircraft Evaluation

3.3.1 Flight Time Estimate

A rough maximum flight time estimation can be obtained from the battery specifications and the average current draw during flight.

The cell voltage of a LiPo battery is 4.2 volts when fully charged, and 3.3 volts when fully depleted. The battery cell voltage should never be outside of this range to prevent risk of damage. A balanced LiPo charger is used to charge the battery to 4.2 V. During flight, the flight controller is programmed to land when the cell voltage is within 0.1 V of the minimum voltage of 3.3 V. LiPo batteries also experience voltage sag (ΔV_{sag}) when supplying power, which decreases battery

efficiency. The higher the current draw, the larger the voltage sag. Voltage sag leads to battery inefficiency, as the voltage sag was measured to be 0.2 V. A battery inefficiency factor can be calculated based on voltage sag and unused battery power under the assumption that current draw is not affected by cell voltage:

$$\eta = 1 - \frac{\Delta V_{sag} + \Delta V_{unused}}{\Delta V_{total}} = 1 - \frac{0.2V + 0.1V}{4.2V - 3.3V} = 1 - 0.33 = 0.67$$

Total flight time can now be calculated by the ratio of the batteries 1C current draw[2] of 5.5 A, and the vehicle's average current draw of approximately 16 A during flight (Table B.2), multiplied by an efficiency factor η.

$$T_{flight} = (60\,\text{min})\frac{I_{1C}}{I_{total}}\eta = (60\,\text{min})\frac{5.5\ A}{14.6\ A}(.67) = 15.1\ \text{min}$$

Later flight tests confirmed flight time is slightly over 15 minutes.

Further inefficiencies are incurred during outdoor operation, as the vehicle needs to utilize battery power to overcome wind loading and other aerodynamical forces and disturbances. More aggressive flights that require frequent accelerations, will also consume a higher average power. These factors will lead to reduced flight time, but were not estimated because the majority of flights the vehicle was hovering indoors.

[2]1C current draw is the amount of current it takes to deplete the fully charged battery in 1 hour

3.3.2 Thrust-to-Weight Ratio

The two most important metrics for evaluating aircraft performance and airworthiness are TWR and disk loading. Disk loading is an indicator of propulsion efficiency. Since this thesis does not involve propulsion system design, disk loading is not analyzed. TWR is analyzed because it involves analyzing how vehicle performance decreases as gross vehicle weight increases. This is an important metric for weight budgeting and battery selection. TWR is a measure of the strain the vehicle propulsion system will experience during flight [34]. TWR is calculated by dividing the maximum thrust the vehicle propulsion system is able to produce by the gross vehicle weight [35].

$$TWR = \frac{F_T}{M_g} = \frac{4.8kg}{2.2kg} = 2.1 \tag{3.1}$$

The higher the TWR, the greater the acceleration, top speed, and responsiveness of the vehicle [34]. While higher TWR provides better flight performance, it requires a higher performance propulsion system which is typically more expensive. Furthermore, increasing the vehicle's maximum thrust typically increases the maximum peak power consumption which the onboard power source may not be able to provide.

A reasonable target for TWR may be determined via the propulsion system specifications for maximum thrust and recommended MGTW. At sea level, the E310 system is capable of producing a maximum thrust of 800 g/rotor with 12V supply voltage. The higher supply voltage of a 4S LiPo battery (14.8 V nominal), will slightly increase the maximum thrust per rotor, the 800 g/rotor is used for

calculations because it serves as a safe lower bound of the vehicles maximum thrust capability. The recommended takeoff weight for an E310 system is 400 g/rotor with a 4S LiPo battery, which produces a target TWR of 2 for with a 4S LiPo battery. The vehicle's TWR of 2.1 is slightly above the recommended TWR of 2.0. This TWR is fairly close to ideal, and it shows that that the vehicle can support a slightly heavier payload if needed.

4. Antenna and Radiation Pattern

This chapter explains how the electrically reconfigurable antenna is mounted on the UAV and controlled by the SDR system. Radiation pattern of the antenna's directional modes that were measured in DWSL's anechoic chamber (Figure 4.4) are presented in this chapter.

The reconfigurable antenna consists of four dipole elements, forming a square shape outline while fed from the center of the square through quasi-microstrip lines (Figure 4.1) [3]. By using PIN diode switches, each element can be switched on or off via control signals directly from the USRP B200mini GPIO pins. There are totally 5 selectable modes including 1 omni-directional mode and 4 directional

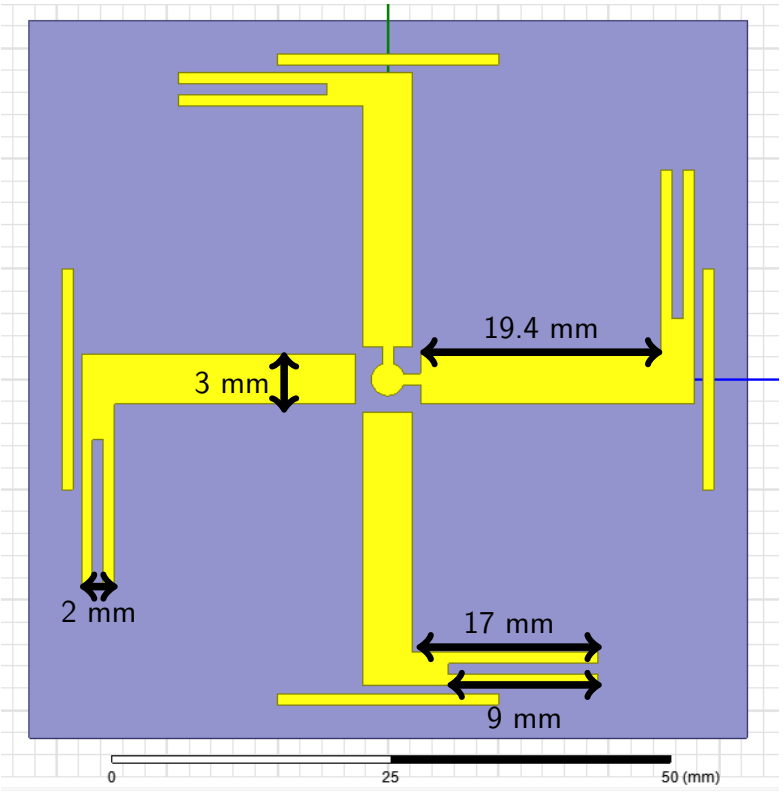

FIGURE 4.1: Antenna Diagram

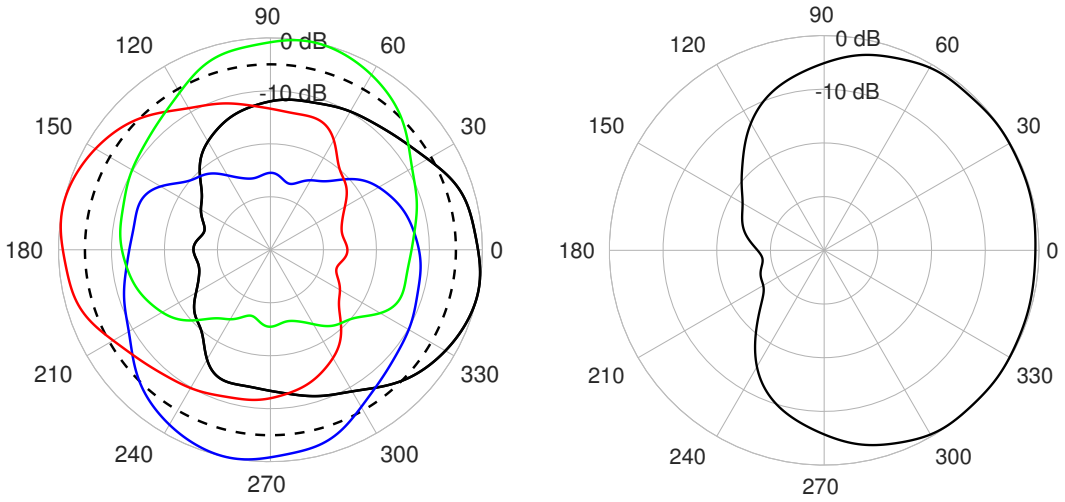

(A) Azimuth (B) Elevation

FIGURE 4.2: Simulated Alford Loop antenna normalized radiation patterns for directional modes

modes. While all the elements are switched on, the antenna is configured as an Alford Loop antenna working in a horizontally polarized omni-directional mode, as recommended by [13], with a maximum gain of approximately 2 dBi. While switching on two adjacent elements, the antenna is operating in a directional antenna mode with maximum gain of about 3.5 dBi and front to back ratio larger than 10 dB. The radiation pattern for directional modes can be rotated horizontally 90 degree increments by selecting different adjacent element pairs (Figure 4.2a).

The antenna is mounted horizontally on the underbelly of the UAV by a cardboard tube that extends 10.5 cm below the lower airframe plate (Figure 4.3). The lower plate is also serves a Power Distribution Board (PDB) PCB which routes battery power to the base of each rotor arm (Figure 3.3). The antenna is horizontally planar, but since the antenna is mounted on UAV with a metallic environment of the PDB module above, the radiated field is reflected by the ground layer of metal board so that maximum gain does not appear in the horizontal plane, but about 45 degree downwards to the ground (Figure 4.5b), unlike the originally

proposed antenna in [3] (Figure 4.2b).

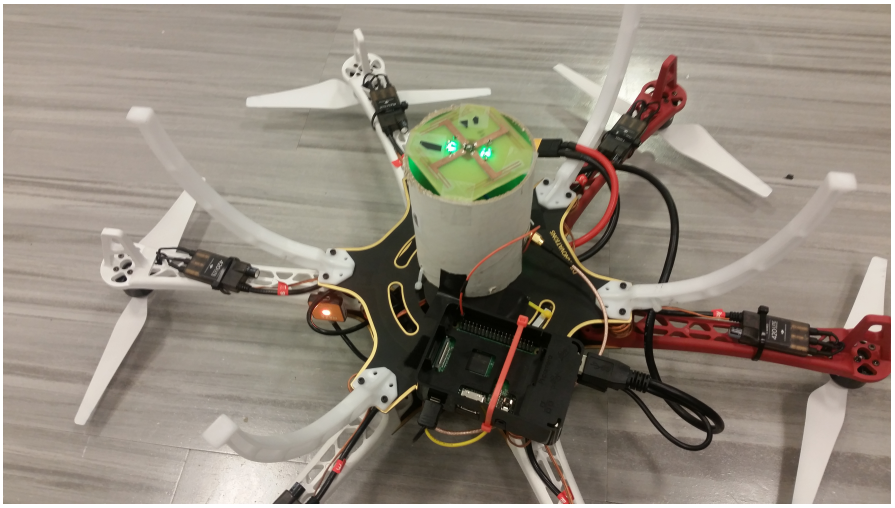

FIGURE 4.3: Alford Loop antenna mounting

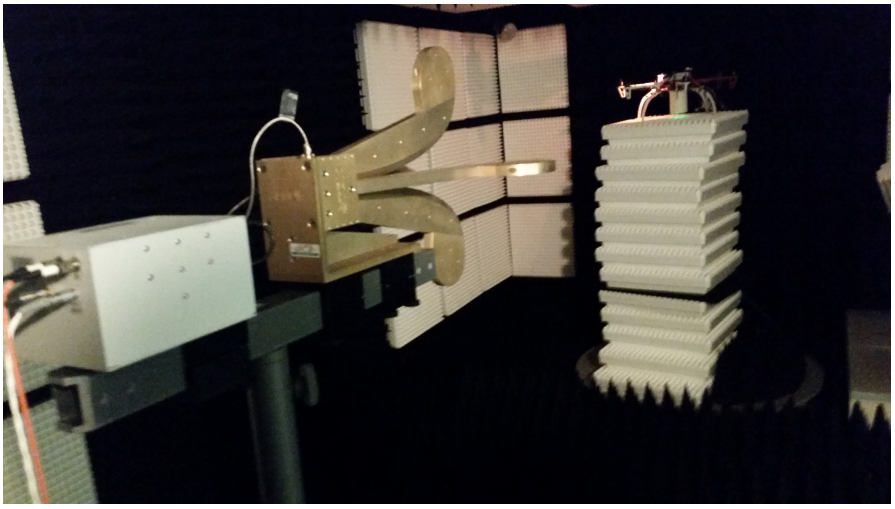

FIGURE 4.4: Measuring reconfigurable antenna's azimuth pattern in DWSL's anechoic chamber when mounted on the UAV.

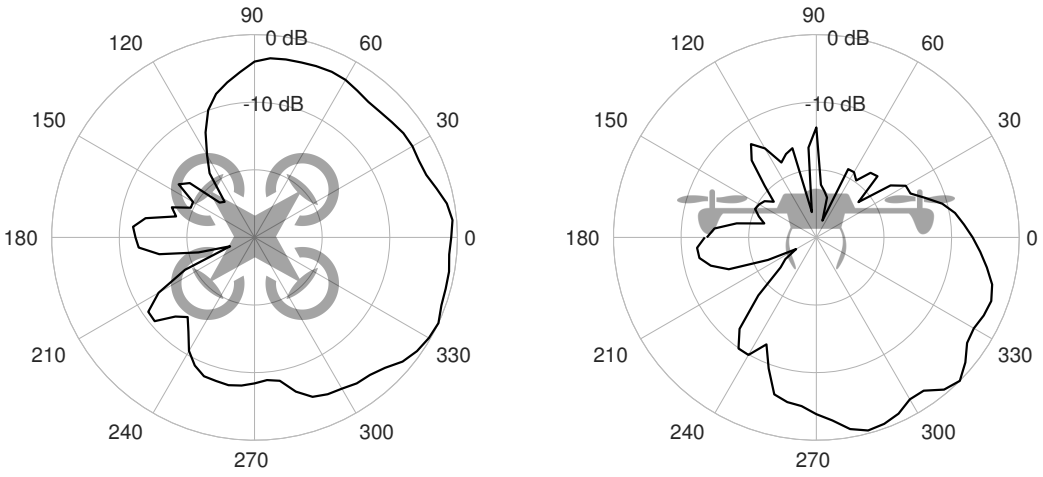

(A) Azimuth (B) Elevation

FIGURE 4.5: Normalized radiation pattern of antenna's directional state when mounted on UAV. The relative orientation of the UAV is shown in gray.

5. Channel Estimation

The implemented antenna selection algorithm attempts to select antenna modes in a manner to increase average SNR which must be estimated on the receiver in an 802.11 compliant manner. The SNR estimation approach is tied into the channel estimation portion of the receiver. This chapter explains how channel estimation and equalization are performed with the least-squares (LS) method described in [36], and how SNR estimation is derived from the CSI. This chapter also analyzes the performances of LS channel estimation and SNR estimation via MATLAB simulation.

LS channel estimation is the simplest to implement and is the most common benchmark for 802.11 channel equalizers. There are more complex dynamic channel estimation and equalization methods for 802.11 vehicle-to-vehicle channels that utilizes data symbols to adapt to CSI variations throughout the frame duration [36]. Most of these methods still utilize the LS technique for initial CSI estimates from the 802.11 preamble.

Since experimental results do not utilize payload symbols, the LS equalizer was used for speed and simplicity. The link optimization methodology will work with more complex channel estimation methods.

5.1 Channel Estimation and Equalization

The LS channel estimation and equalization technique utilizes the LTS portion of the 802.11 preamble. There are two LTS symbols, each transmitting a known symbol on all 52 utilized subcarriers. The DFT of these symbols are $Y_1(k)$ and $Y_2(k)$, which are calculated via Equation 2.2. The goal of channel estimation

is to estimate CSI, $H(k)$, for each subcarrier based on Equation 2.3. As mentioned in Section 2.2 the LS channel estimation method assumes the frame duration is well within the coherence time of the channel[1]. Therefore, the channel estimate can be considered to be constant for the duration of the OFDM frame.

The first equalization step is to estimate the received LTS constellation point, $\bar{Y}_i(k) = H(k)\, X_i(k)$, which is the received LTS constellation point when no noise is present in the channel. Since $Y_i\,(k)$ is the sum of a constant, $H(k)\, X_i(k)$, and AWGN noise, $W(k)$ with variance $N(k)$, has a probability density function with the following distribution:

$$Y_i(k) \sim \mathcal{N}_c\left(H(k)\, X_i(k)\,, N(k)\right) \tag{5.1}$$

Since $Y_i(k)$ is normally distributed, the maximum likelihood estimate for $\bar{Y}(k)$ is the mean of the received LTS constellation points.

$$\hat{\bar{Y}}\,(k) = \mathbb{E}\left[\bar{Y}\,(k)\mid Y_1\,(k)\,,\, Y_2\,(k)\right] = \frac{Y_1\,(k) + Y_2\,(k)}{2}$$

For the pilot frames $X_i(k)$ is known and $X_1(k) = X_2(k)$, therefore we can then estimate the subcarrier CSI:

$$\hat{H}(k) = \frac{\hat{\bar{Y}}_i(k)}{X(k)} = \frac{Y_1(k) + Y_2(k)}{2X(k)} \tag{5.2}$$

[1]Research in mobile ground vehicle channels suggest this is may not always true when vehicles are moving at high speeds where Doppler effects are significant. Requiring a more advanced equalizer [36]. In these scenarios Average EVM Squared (AEVMS)-based SNR estimation described in [37] can be implemented with minimal change to the beamsteering methodology

Equalization is performed on the following payload symbols by dividing the received symbol by the estimated subcarrier CSI:

$$\hat{X}_i(k) = \frac{1}{\hat{H}(k)} \left[H(k)\, X_i(k) + W(k) \right] \quad i > 2 \tag{5.3}$$

5.2 SNR Estimation

It is possible to estimate signal power is from the CSI magnitude, and noise power can be estimated by Error Vector Magnitude (EVM) of the received LTS symbols. SNR can then be estimated by dividing the signal power estimate by the noise power estimate. Due to receiver gains applied to the signal it is not possible to estimate raw signal and noise power at this stage of the receiver. The estimated signal power (S) and noise power (N) are not the *true* estimates. Since the same gains are applied to both the signal and noise, the relative magnitude of power estimates are still accurate. Therefore SNR can still be accurately estimated.

The subcarrier received signal amplitude was estimated to be $|\hat{H}(k)|$. Therefore, the subcarrier signal power, $S_i(k)$, can be estimated as:

$$\hat{S}(k) = |\hat{H}(k)|^2 \tag{5.4}$$

The subcarrier noise power estimate, $\hat{N}(k)$, is obtained from difference between $Y_1(k)$ and $Y_2(k)$. Equation 5.1 shows that the received LTS constellation points, $Y_i(k)$, has a complex normal distribution with a variance of $N(k)$. The difference between the two received LTS constellation points $Y_1(k)$ and $Y_2(k)$ is also has a complex normal distribution with variance of $2N(k)$.

$$Y_1(k) - Y_2(k) \sim \mathcal{N}_c\left(0, 2N(k)\right)$$

The squared magnitude of the difference between the two received LTS constellation points is then exponentially distributed:

$$|Y_1(k) - Y_2(k)|^2 \sim \text{Expo}\left(\frac{1}{4N(k)}\right)$$

The expected value of an exponentially distributed random variable with rate parameter $\frac{1}{4N(k)}$ is $4N(k)$, therefore:

$$\mathbb{E}\left[|Y_1(k) - Y_2(k)|^2\right] = 4N(k)$$

As a result, the subcarrier noise power can be estimated via:

$$\hat{N}(k) = \frac{1}{4}\left(|Y_1(k) - Y_2(k)|^2\right) \tag{5.5}$$

Total SNR can be estimated by summing noise power and signal power over all 52 subcarriers and dividing the results:

$$
\begin{aligned}
SNR &= \frac{\sum_{k=1}^{52} \hat{S}(k)}{\sum_{k=1}^{52} \hat{N}(k)} \\
&= 4\frac{\sum_{k=1}^{52} |\frac{Y_1(k)+Y_2(k)}{2X(k)}|^2}{\sum_{k=1}^{52} |Y_1(k) - Y_2(k)|^2} \\
&= \frac{\sum_{k=1}^{52} |Y_1(k) + Y_2(k)|^2}{\sum_{k=1}^{52} |Y_1(k) - Y_2(k)|^2}
\end{aligned} \tag{5.6}
$$

5.3 Simulated SNR Estimate Performance

The LS-based SNR estimation was simulated for 30 true SNR values ranging from -10 dB to 20 dB. At each SNR value, 10,000 SNR estimates were obtained under the previously described channel model (Equation 2.3) and SNR estimation method (Equation 5.6). It is important to determine how the SNR estimation performs in both high multipath conditions and high LOS conditions[2]. The simulation evaluates the performance of SNR estimation under a under various Rician K-factors.

5.3.1 Least-Squares Estimation Bias

While SNR estimation may have bias and measurement error, it is critically important that the expected SNR estimate under channels with different Rician K-factors are equal under a given true SNR as the adaptive beamsteering algorithm will need to compare SNR estimates between antenna modes with varying degrees of LOS components.

[2]In reality, the fading model will contain both LOS and multipath components. This simulation analyzes the two extremes to show best-case and worst-case channel conditions.

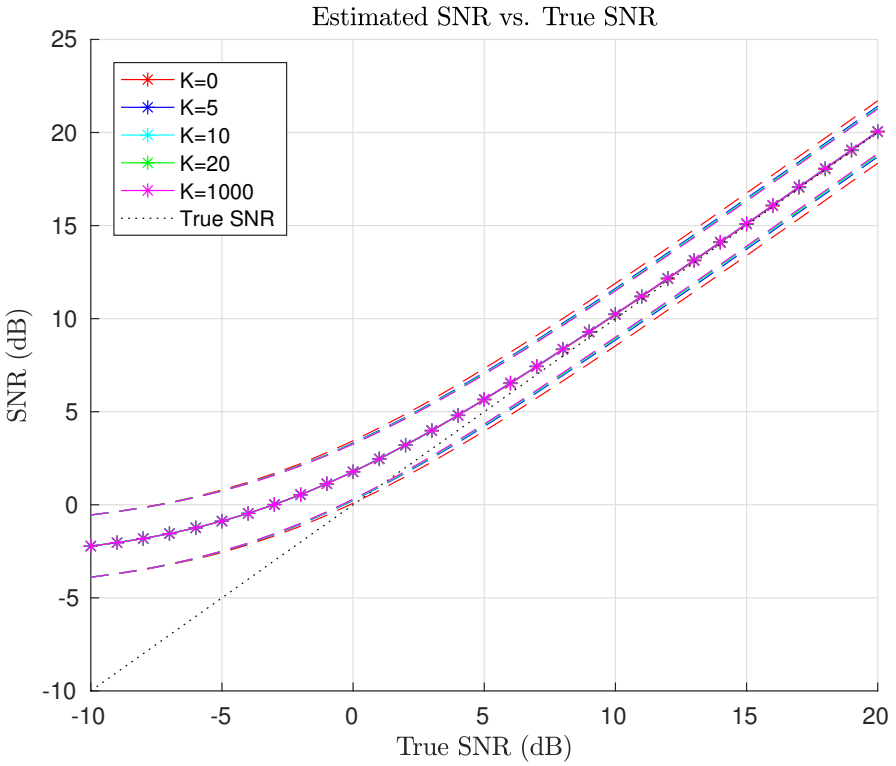

FIGURE 5.1: LS equalizer SNR estimate bias and 90% confidence intervals in various Rician K-factor channels

The bias was estimated by taking the mean of SNR estimates at various true SNR values (Figure 5.1). The simulation results show that in low SNR conditions, noise has a significant effect on the received symbols. This often causes signal power estimates, and therefore SNR estimates, to be overestimated by the LS equalizer. At SNR values above 5 dB, the bias is small and can be considered negligible in the context of antenna selection algorithms. Considering the minimum SNR to maintain a link is typically around 10 dB, the bias is negligible at all SNR values high enough to maintain a stable link. Experimental measurements in this thesis were conducted in channel conditions where the mean SNR was in the range of 13-25 dB.

5.3.2 Least-Squares Estimation Error

It is important to see if the variance in SNR estimates change as true SNR changes. the variance in SNR estimates was calculated for each true SNR value and graphed (Figure 5.2).

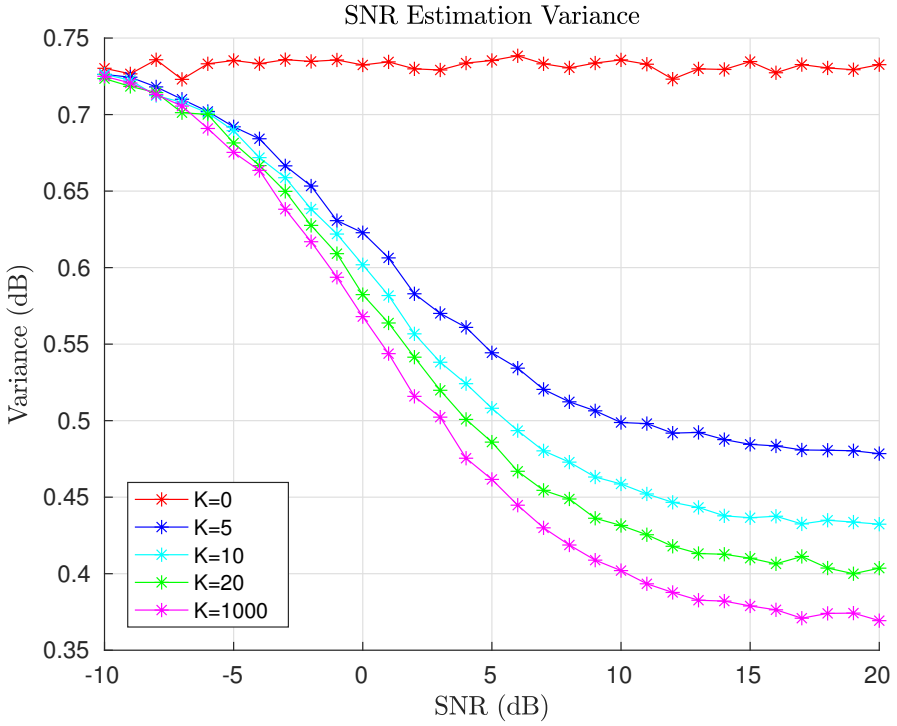

FIGURE 5.2: LS equalizer SNR estimate variance in various Rician K-factor channels

The variance in SNR estimates under K=0 fading model appears to be unaffected by changes in true SNR. This means that distribution in estimated SNR will have a variance of approximately 0.73 dB, for all true SNR values. Under a Rician fading model, SNR estimation variance decreases from 0.73 to 0.37 dB as true SNR increases. Since SNR is above 10 dB most experimental results, SNR estimation variance can be expected to be in the range of 0.37-0.40 dB.

To get an idea of the probability density function of SNR estimates, a histogram of the equalizer estimate error was obtained via simulation at a true SNR

of 20 dB where the estimation bias was negligible. The SNR estimation error histogram under $K = 0$ Rician (Figure 5.3a) and $K = 1000$ Rician (Figure 5.3b) fading models show that SNR estimation is approximately normal. Overall, the simulation results show that SNR estimation works best under high K-factor Rician fading with a high SNR. Realistically, the fading distribution observed at each antenna mode be somewhere between the $K = 0$ Rician and $K = 1000$ Rician models. Therefore SNR estimation performance best-case and worst-case performance can be bounded by these two models.

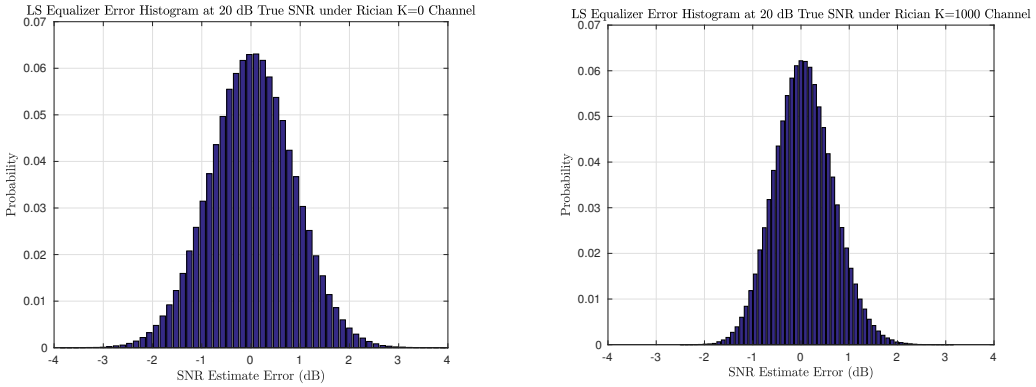

(A) K=0 Rician (B) K=1000 Rician

FIGURE 5.3: Simulated histogram of LS equalizer SNR estimate error at a true 20 dB SNR in various Rician K-factor channels

6. Antenna Selection Algorithm

The reconfigurable antenna modes allow the onboard UAV radio to steer the directional antenna radiation pattern described in Chapter 4 in four different directions. At a given time in flight, some modes will provide a higher link quality than others (Figure 6.1). The goal of link optimization via reconfigurable antenna mode selection is to learn and exploit the reconfigurable antenna mode provides the best link quality. The link optimization is done in an adaptive manner because the best antenna mode may change during flight due changing channel conditions

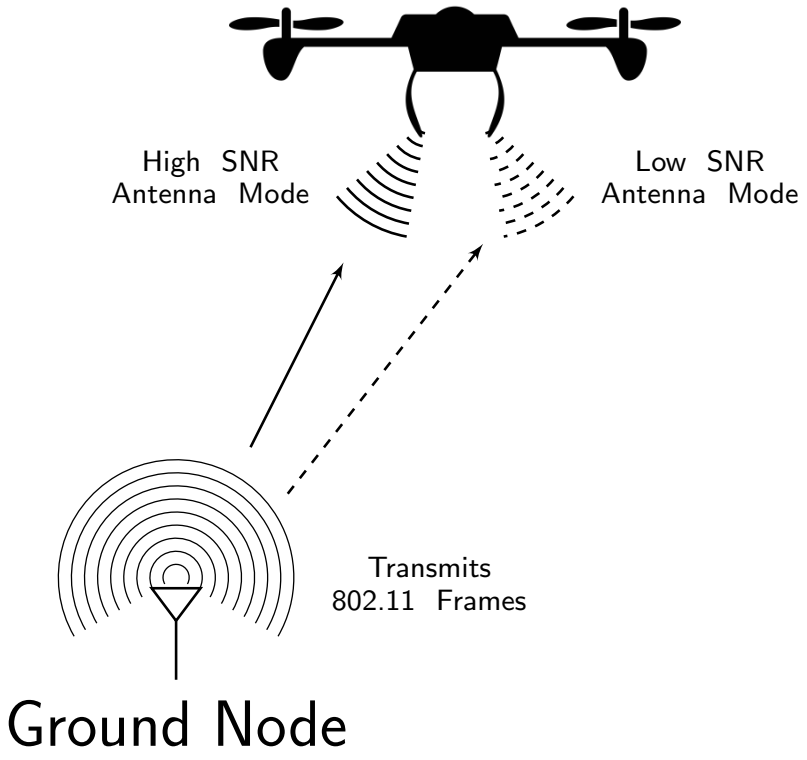

FIGURE 6.1: Link optimization concept diagram

and movements of the UAV and/or ground node. The key challenge in effectively integrating reconfigurable antennas into practical wireless systems is the selection of an optimal radiation pattern among all available patterns for a transceiver in a given wireless environment.

The selection of the optimal mode requires additional channel state information (CSI) for each antenna mode and the overhead associated with obtaining complete and instantaneous CSI can be significant due to mobility, changes in the antenna orientation and the dynamic nature of the wireless channel. To address these challenges, an online learning approach is adopted for reconfigurable antenna mode selection based on Multi-Armed Bandit (MAB) theory presented in [18].

The MAB problem is a classic reinforcement learning problem, where an agent chooses a sequence of mutually exclusive actions that are each associated with a stochastic reward in the hopes of maximizing the cumulative reward over time. In the context of wireless link optimization, the set of antenna patterns make up the K possible actions and the received signal-to-noise ratio (SNR) estimate is the reward associated with each action.

Due to movements by the UAV and changes in the environment, the SNR distribution, and therefore reward distribution at each antenna mode is time-varying. An selection policy called *adaptive pursuit* (AP) is an adaptive strategy that is designed for non-stationary MAB problems where reward distributions are time-varying [21]. The AP strategy has been previously used to optimize wireless link quality using signal-to-interference-and-noise ratio (SINR) as reward in the context of interference alignment [19]. However, to the best of our knowledge, this approach has not been utilized in mobile (or aerial) environments.

The AP strategy is an psuedo Expectation-Maximization approach. The goal of the AP strategy is to adapt an *arm selection probability vector* ($\mathbf{P}$), containing the probability of selecting each antenna mode (arm), to increase the probability of selecting the estimated best arm. The expected reward from each arm is tracked by an *arm quality vector* ($\mathbf{Q}$), which is updated every time a new reward (i.e. SNR measurement) is obtained. The arm with the highest expected reward is considered the best arm. The AP is a recursive strategy, where on each iteration a random arm i is chosen based on the distribution determined by $\mathbf{P}$. An $R_i[n]$ is obtained from the selected arm. The algorithm updates the expected future reward for selected arm via a first-order low pass filter.

$$Q_i[n+1] = (1-\alpha)\, Q_i[n] + \alpha R_i[n]$$

Where $i \in \{1, \cdots, K\}$, and quality adaption rate is controlled by $\alpha : 0 < \alpha \leq 1$.

The arm selection probability vector $\mathbf{P}$ is then updated to increase the selection probability of the arm with the highest expected quality (i^*), and decrease the probability of selecting other arms. It is undesirable for an arm's selection probability to be extremely low as this would prevent the algorithm from exploring that arm, so a restriction is imposed which requires the selection probability of any given arm to be no less than P_{min}. The probability vector $\mathbf{P}$ is updated in the following manner, which increases the probability of selecting i^*, but also enforces the minimum arm selection probability constraint.

$$P_i[n+1] = \begin{cases} P_i[n] - \beta\left(P_{max} - P_i[n]\right) & i = i^* \\ P_i[n] - \beta\left(P_{min} - P_i[n]\right) & \text{else} \end{cases}$$

The probability adaption rate is determined by $\beta : 0 < \beta \leq 1$. To ensure total probability of selecting all states is unity:

$$P_{max} = 1 - (K-1)\,P_{min}$$

The selection of P_{min} controls the tradeoff between exploiting the arm and exploring other arms. The AP strategy will exploit the best state with a maximum probability P_{max}, and explore each other state with a minimum probability of P_{min}. The selection of adaption rates α and β control how quickly the AP strategy will adapt it's quality vector and probability vector to changing arm reward distributions. α determines how much previous reward measurements contribute to the current quality estimate. β controls the greediness of the algorithm as it determines how rapidly the selection distribution will adapt to a change in i^* . The entire AP policy is shown in Algorithm 1.

The UAV implementation of AP strategy for adaptive beamsteering uses the 802.11 SDR PHY implementation [22] to receive the 802.11 frames. The reward is calculated by SNR estimator analyzed in Chapter 5, and the output of the AP policy controls the reconfigurable antenna state (Figure 6.2)

The received SNR estimate was chosen as the quality metric because it can be estimated on the receiver from the magnitude and Error Vector Magnitude (EVM) of the received symbols in the Long Training Sequence (LTS) portion of the 802.11

Algorithm 1 Adaptive Pursuit

function AdaptivePursuit($\mathcal{P}, \mathcal{Q}, K, P_{min}, \alpha, \beta$)
  $P_{max} \leftarrow 1 - (K-1) P_{min}$
  for $i \leftarrow 1$ **to** K **do**
    $\mathcal{P}(i) \leftarrow \frac{1}{K}$; $\mathcal{Q}(i) \leftarrow 1.0$
  while NotTerminated?() **do**
    $a^s \leftarrow$ ProportionalSelectOperator($\mathcal{P}$)
    $R_{a^s}(t) \leftarrow$ GetReward(a^s)
    $\mathcal{Q}_{a^s}(t+1) = \mathcal{Q}_{a^s}(t) + \alpha [\mathcal{R}_{a^s}(t) - \mathcal{Q}_{a^s}(t)]$
    $a^* \leftarrow \text{argmax}_a (\mathcal{Q}_a(t+1))$
    $\mathcal{P}_{a^*}(t+1) = \mathcal{P}_{a^*}(t) + \beta [P_{max} - \mathcal{P}_{a^*}(t)]$
    for $a \leftarrow 1$ **to** K **do**
      if $a \neq a^*$ **then**
        $\mathcal{P}_a(t+1) = \mathcal{P}_a(t) + \beta [P_{min} - \mathcal{P}_a(t)]$

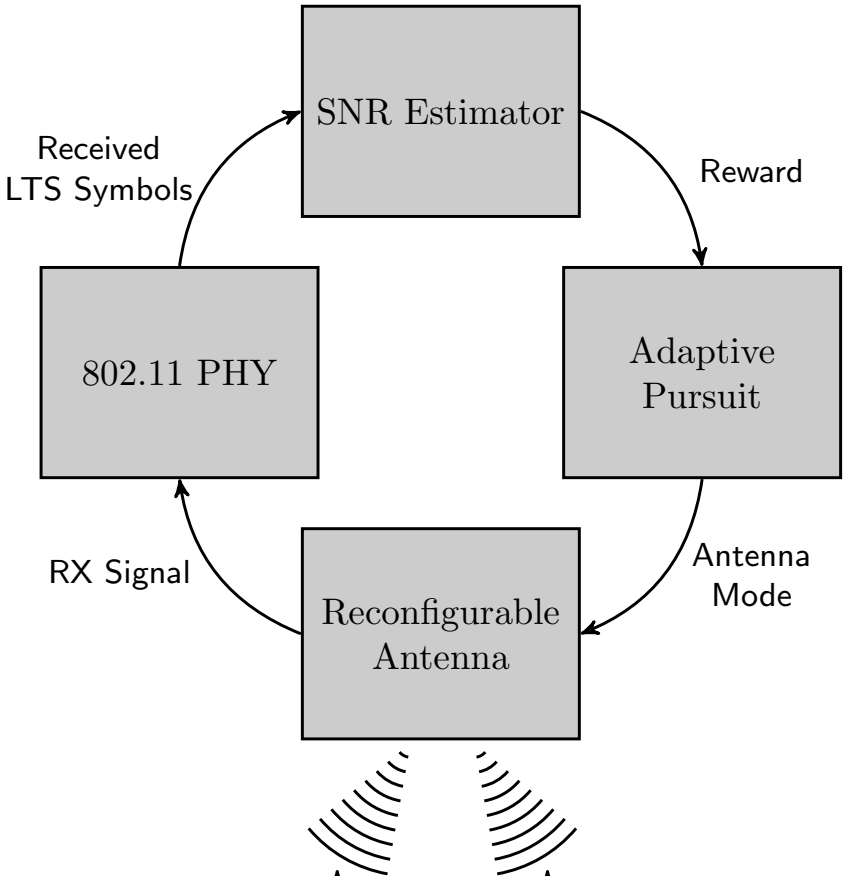

Figure 6.2: Onboard adaptive antenna selection flow diagram

preamble, and therefore does not require any additional overhead. SNR estimation is explained in great detail in Chapter 5. Also, higher SNR directly corresponds

to lower BER rates, which will very likely lead to an increase in throughput.

The current antenna mode selection implementation only optimizes the ground-to-UAV link, and the reverse link is not analyzed in this thesis. However, because the system operates in a Time Division Duplex (TDD) mode, it is reasonable to assume reciprocity between the uplink and downlink channels. Thus, at each time instant the best antenna mode for the ground-to-UAV and UAV-to-ground links will be the same.

6.1 Antenna Mode Selection Policy Discussion

Adaptive Pursuit was the chosen antenna mode selection policy and is the only policy that is implemented in an online manner. However, it is important to discuss other more commonly used policies.

6.1.1 ϵ-greedy Policy

A common strategy for non-stationary MAB problems is a selection policy called ϵ-greedy. This policy maintains a quality vector reward-based update Adaptive Pursuit's $\mathbf{Q}$ vector. However, rather than maintaining an arm selection distribution vector $\mathbf{P}$, ϵ-greedy selects the best arm (i^*) with probability $1 - \epsilon$ and selects a random arm (with uniform probability) with probability ϵ. The parameter ϵ in the ϵ-greedy policy determines the tradeoff between exploration and exploitation, and is very similar to AP's parameter P_{min}.

The main difference between ϵ-greedy and AP policies is the transient behavior of arm selection probabilities when there is a change in the best arm (i^*). When the best arm changes, both algorithms will *reconverge* their selection probabilities to increase the probability of selecting the new best arm. ϵ-greedy does this reconvergence instantaneously, while AP selection probability more *slowly* adapts

at a rate governed by the β parameter. AP policy with β=1 is effectively the same as the ϵ-greedy policy. When AP has converged to steady-state[1], its arm selection distribution is identical to ϵ-greedy, where $P_{min} = \frac{\epsilon}{K}$.

High exploration rates can lead to decreased cumulative reward due to the increased probability of selecting arms that yield poor rewards. However, high exploitation rates causes the policy to have less accurate expected reward for each arm, which increases the chance of exploiting the sub-optimal arm. It is often desirable to decrease ϵ when the reward distributions are relatively stationary, and increase ϵ when there is uncertainty in the arm quality estimates. This is called an *adaptive ϵ-greedy* policy. AP is similar to an adaptive ϵ-greedy strategy as the arm with the highest selection probability will be decreases when there is higher *uncertainty* in the best arm.

While it is expected that an adaptive ϵ-greedy and AP policies will provide fairly similar performance (and will also likely outperform traditional ϵ-greedy for beamsteering application), the primary reason AP policy was chosen for UAV beamsteering is because it has been previously utilized for terrestrial antenna wireless beamsteering experiments [19].

6.1.2 Non-Reinforcement Learning Approaches

Other non-reinforcement learning-based strategies could be implemented for antenna mode selection in UAV-to-ground communications. The most obvious strategy, which will be referred to as the *straw man* policy, would be to always utilize the antenna mode that points in the direction of the ground node (i.e. the

[1]This occurs when the best arm has not changed for a relatively long period of time, so it's selection probability is near P_{max} and the selection probability of all other arms are near P_{min}.

"LOS" antenna mode[2]). Unlike reinforcement learning approaches to beamsteering straw man policy makes a *naive* assumption that the best antenna orientation points in the direction of the ground node, this is a reasonable assumption in low multipath LOS channels, and was a core assumption in UAV-to-UAV communication research [12]. The straw man policy does not have any exploration penalty, and therefore may outperform reinforcement learning-based beamsteering algorithms in these scenarios. However, the LOS antenna mode is not always the best antenna mode. This is especially true in short-distance low-altitude UAV-to-ground links analyzed in this thesis which are more likely to have high multipath and/or NLOS channel conditions. In addition, channel situations involving co-channel interference or jamming may also cause relatively poor performance on the LOS antenna mode.

Perhaps the biggest drawback to the straw man policy is that additional sensors and data overhead are required to determine the direction of the ground node with respect to the orientation of the UAV. A GPS and magnetometer onboard the UAV that is accessible by the onboard radio is required to establish a reference frame based on the position and heading of the UAV. To determine the direction of the ground node in respect to the UAV's frame of reference, the ground node will also need a GPS and must send the UAV it's GPS position, thus increasing data overhead.

The straw man policy selects antenna modes based on the relative orientation of the ground node measured by sensor data. While the limitations of the straw man policy have been discussed, the idea of using onboard sensor data for

[2]This "LOS" antenna mode may not provide true line-of-sight as it's possible an obstacle is interfering with the LOS path

beamsteering algorithms can be adapted to for use in the reinforcement learning-based beamsteering algorithms. Even if the UAV doesn't have a GPS, the at least has an IMU (Inertial Measurement Unit) which consists of a gyroscope and accelerometer[3]. It is possible to use this sensor data to tune the exploration/exploitation tradeoff in an online fashion. When the UAV moves, it is likely that the reward distributions at each antenna mode change. Sensor data could be used to detect increase the exploration rate when the UAV is undergoing movement and maneuvers, and decrease the exploration rate when the UAV has been stationary for a relatively long period of time. This thesis does not experiment with fusing the UAV's onboard sensors with the beamsteering policy to further improve link performance, however this is an avenue for future work.

[3]Technically, only a gyroscope is needed to achieve stable controlled flight. However, without an accelerometer the vehicle attitude needs to be manually controlled by the pilot.

7. Indoor Experimental Setup

Initial experiments were conducted indoors in the arena of the Drexel MESS Lab which allowed for more controlled experiments where aerodynamic disturbances such as wind are minimal. These experiments were used to characterize the SNR distributions at each antenna mode in both flight and non-flight scenarios, tune the AP policy via post-processing methods using the measured in-flight SNR data, then test and evaluate how well the adaptive beamsteering algorithm performs under various scenarios.

7.1 Experimental Setup

The performance of the AP policy and omni-directional antenna are compared in an indoor environment under various situations. All indoor experimentation was performed in a large indoor 38 ft. by 44 ft. open space with a ceiling height of approximately 20 ft. The indoor space has a grid scaffolding structure at a height of 12 ft.

The ground transmitter node consisted of a USRP N210 [30] with a Lenovo Thinkpad W520 host. The implementation was using the gr-ieee802-11 GNU Radio recipe to transmit an OFDM frame at 10 ms intervals using a 2.4 GHz omni-directional monopole antenna. The frame structure is compliant with the IEEE 802.11a/g/p standards, however due to the limited processing power of the Raspberry Pi 3, the frames use a sampling rate of 5 MHz instead of 20 MHz. All ODFM data subcarriers used the BPSK modulation format. WiFi channel 14 was utilized for the experimental ground-to-UAV link to avoid interference from the UAV control link or any other wireless devices.

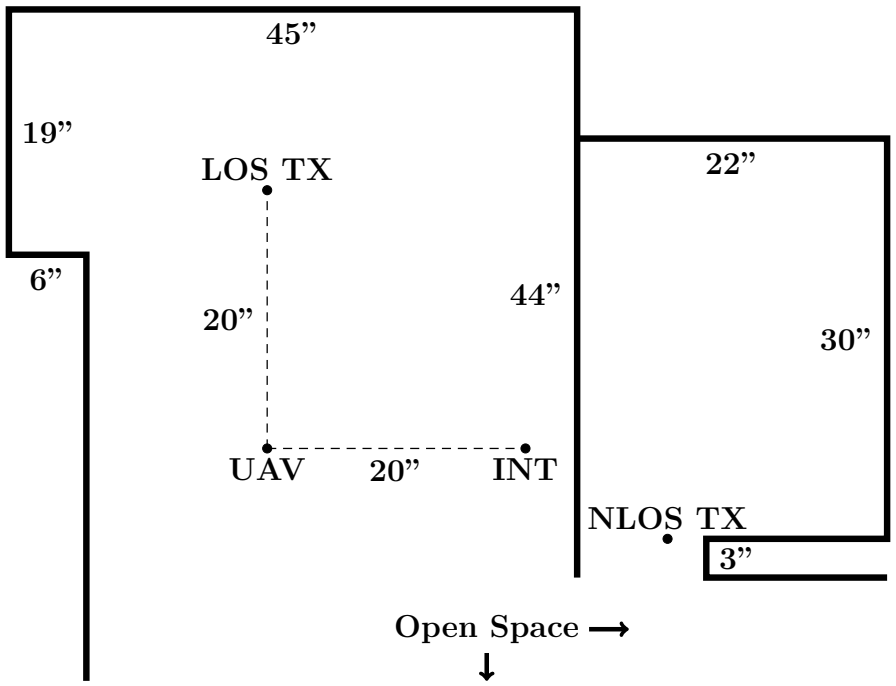

FIGURE 7.1: Indoor experimental layout showing flight position (UAV), transmitter position (LOS TX), NLOS transmitter position (NLOS TX), and interference source position (INT)

The UAV's SDR system ran the physical layer of the GNU Radio IEEE 802.11 receiver, which was modified to control the reconfigurable antenna state and log SNR measurements [22]. The antenna control and SNR logging was implemented in a separate thread, which would run the AP policy utilizing the most recently measured SNR every 150 ms.

7.2 Channel SNR Characterization

Before implementing online adaptive antenna selection policies, the SNR distribution under both flight and non-flight scenarios are characterized to show how the ground-to-UAV link characteristics are affected by movement, vibration, propellers, etc.

During channel characterization tests, the onboard radio was programmed

FIGURE 7.2: UAV hanging from ceiling grid during non-flight scenario experiment

to cycle through all five antenna modes (four directional states and one omnidirectional state) in a round-robin manner gathering SNR measurements. This cycling allows SNR distributions for each antenna mode can be characterized under different channel scenarios.

For the non-flight scenario, the UAV was hung by a rope from the ceiling grid approximately 8 ft. above the ground (Figure 7.2). The ground transmitter node was placed on a cart 20 ft. away from the UAV, such that the transmitter antenna is 3 ft. above the ground. This placement creates a 14 degree elevation angle between transmitter's horizon and the UAV (Figure 7.1). The ground node's transmission power was 10 dBm. The propellers were off, therefore the vehicle's position and heading angle were fixed and the vehicle was not subjected to vibration, minor movements, and other aerodynamic effects that occur during UAV flight.

The cumulative distribution function (CDF) for each antenna state is calculated by the channel characterization radio configuration in the non-flight scenario

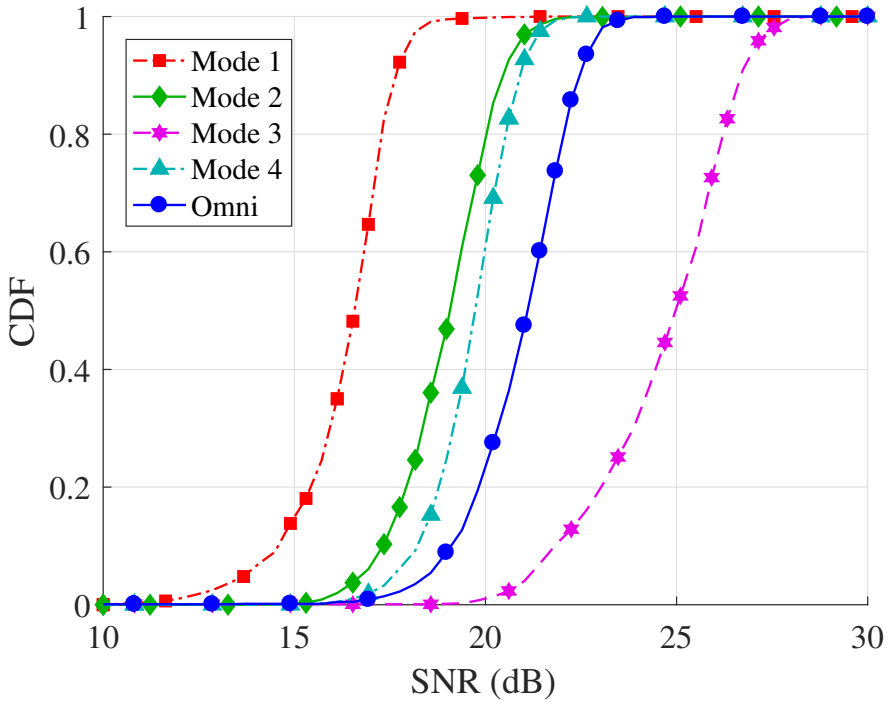

FIGURE 7.3: Antenna mode SNR CDFs during the non-flight scenario

where the UAV is hanging from a rope (Figure 7.3). The mean SNR variance measured at each mode was measured to be 2.6 dB. The difference in mean SNR between the best and worst performing mode was in the range of 8-12 dB. The low variance, and high deviation in mean SNR per arm leads to minimal distribution overlap.

Using the same channel characterization radio configuration and ground transmitter position as before, two 10 minute indoor hover flights were conducted where the pilot tried to keep the vehicle in the same position and heading angle as in the non-flight scenario. The measured SNR distributions during flight show a significantly greater variance in the range of 15-17 dB. There also is a notably smaller difference mean SNR between the best and worst performing mode was in the range of 4-6 dB (Figure 7.4).

The increased variance and decreased mean SNR spread leads to significantly

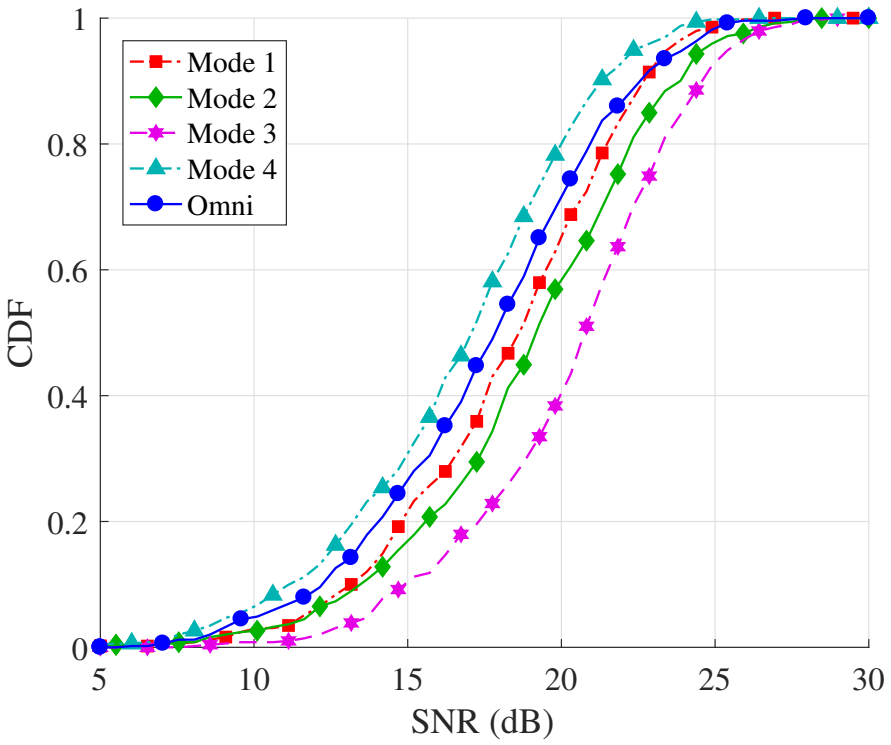

FIGURE 7.4: Antenna mode SNR CDFs during indoor hover flight

more CDF overlap per arm. This makes it more difficult for the adaptive antenna selection policy to distinguish the best state. The adaptive pursuit strategy utilizing similar reward metrics has been previously shown to be able to optimize link quality in scenarios similar to the hanging scenario [19], however the antenna selection policy has not been implemented in mobile or aerial changing environments. These results show that continuous movement of the UAVs antenna reduces the performance of the adaptive beamsteering algorithm.

7.3 Offline Adaptive Pursuit Implementation

The channel characterization data from the hover flights was also applied to the AP and ϵ-greedy policies in a post-processing manner to roughly approximate the policy performance and the tune the adaption parameters. Due to the low sampling rates in the experiment, a 90% exploitation rate was implemented on

both policies ($P_{min} = 0.1$) forcing the strategy to frequently explore states other than i^*.

The AP and ϵ-greedy policies were applied to the SNR data in two different configurations. The first configuration utilized the four directional antenna modes. The second configuration utilized the four directional antenna modes and the omni-directional state. Each configuration was applied to the data one hundred times and the realized mean SNR was averaged and compared to the omni-directional antenna mode.

The offline AP implementation shows an average gain of approximately 0.9 dB SNR gain over omni-directional when using AP with the omni-directional mode, and a 1.2 dB SNR gain when using AP without the omni-directional mode (Figure 7.5). The ϵ-greedy policy produced a 0.6 dB SNR gain over omni-directional, and the optimal antenna selection strategy provides a 4.5 dB SNR gain over omni-directional. The optimal antenna selection shows the absolute best-case performance that any antenna selection policy can produce. This selection policy chooses the antenna state that has the highest SNR on each measurement cycle. The optimal selection policy is impossible to implement in real-time because requires prior knowledge consisting of the realized SNR values at each antenna mode at every time instant.

Measurements show that AP without omni-directional mode slightly outperforms AP with the omni-directional mode. Performance is reduced with the omni-directional state because increasing the number of possible states of the AP strategy increases the required exploration effort, which in turn decreases the exploitation rate. Since it is very unlikely that the omni-directional mode the highest

average SNR in comparison to the directional states, the increased exploration effort rarely results in higher average SNR payoff. As a result, AP without the omni-directional mode is utilized in all online implementations.

The AP parameters used in future online implementations were chosen by tuning the AP strategy without omni-directional offline using the channel characterization data. The tuned parameters were $\alpha = 0.15$ and $\beta = 0.15$ which produced the 1.2 dB offline mean SNR gain shown above.

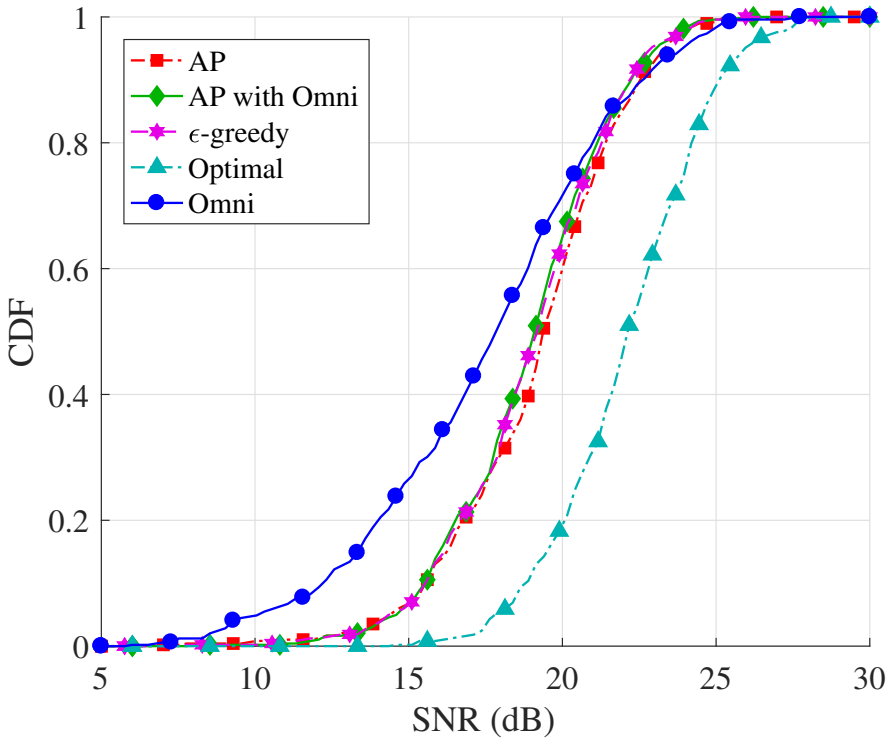

FIGURE 7.5: Offline AP SNR CDFs based on indoor hover flight data

7.4 Online Adaptive Pursuit Implementation

The AP policy was implemented online using the tuned parameters obtained from the offline implementation. Since each UAV flight is a non-static environment and UAV movements are not precise to be perfectly reproduced, the performance of the antenna states and selection policies are ideally compared over the same

flight. The online approach switches between omni-directional mode and the AP policy every 150 ms throughout the duration of the flight.

The AP strategy and the omni-directional antenna mode were implemented in the following scenarios (Figure 7.1).

- **Hover** - Hover flights were conducted in the same manner that the in-flight channel SNR characterization tests were conducted. The only difference is that the SDR payload was running the AP policy instead of logging SNR data.

- **Rotating Hover** - The rotating hover scenario tests how the antenna selection policy adapts to rapid changes in SNR distributions at each antenna mode. A 12 minute flight was conducted in the same manner as the hover scenario, except that the vehicle heading angle was changed by 90 degrees on three minutes intervals.

- **Non-Line of Sight Hover** - The antenna selection policy is tested under NLOS scenario. The NLOS scenario was conducted in the same manner as the hover scenario, except the transmitter node was moved to an adjacent room.

- **Hover with Interference** - A hover flight was conducted in the same manner as the hover scenario, except that an Agilent N5182A vector signal generator was transmitting co-channel QPSK LOS interference at -5 dBm and 5 MHz bandwidth. The transmitter was positioned 3 ft. above the ground approximately 20 ft. away from the UAV at an angle of 90 degrees from the ground transmitter node.

8. Indoor Experiment Results

8.1 Hover Scenario

The experimental results from the hover flight show that the online AP strategy utilizing four directional modes shows a mean SNR gain of 1.23 dB over the omni-directional antenna (Figure 8.1).

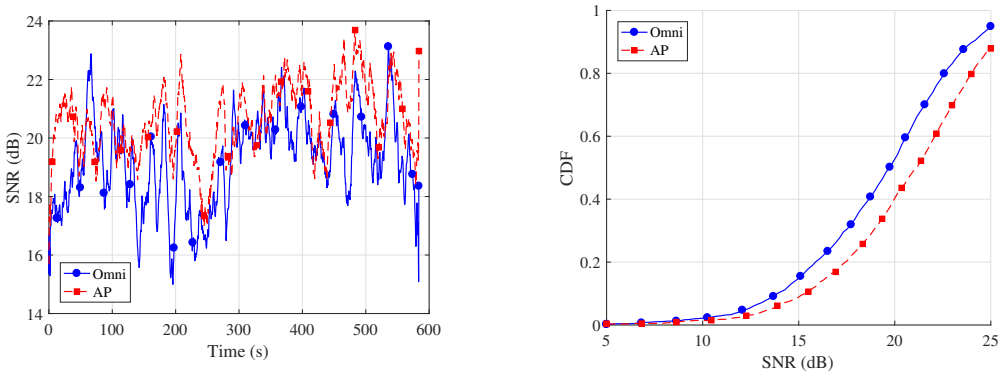

(A) Smoothed SNR measurements

(B) Online AP performance

FIGURE 8.1: Online AP performance during indoor hover scenario

The rotating hover test resulted in a mean SNR gain of 1.1 dB (Figure 8.2). The slight decrease in performance in comparison to the hover scenario likely caused by a decrease in AP performance when the vehicle's heading angle changes due to the significant changes to the SNR distribution at each antenna mode.

8.2 Rotating Hover Scenario and Visualization of the AP Policy Adaption

To visualize how the AP policy adapts to significant changes in reward distributions at each antenna mode, Figure 8.3 shows the normalized frequency that each antenna mode was selected throughout the duration of the hover and rotation hover experiments.

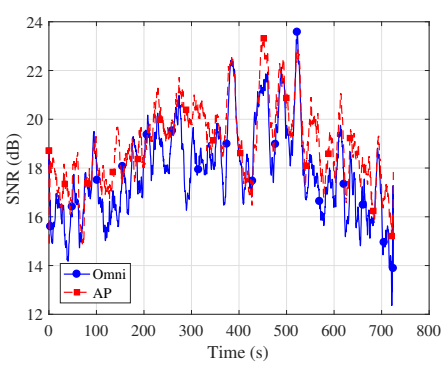

(A) Smoothed SNR measurements

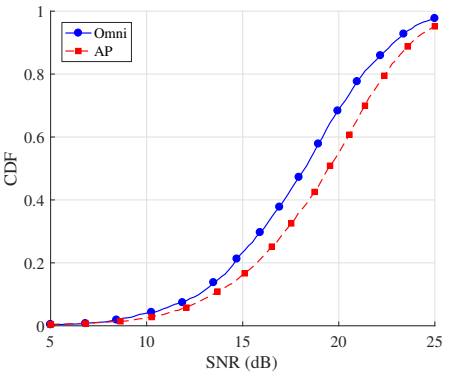

(B) Online AP performance

FIGURE 8.2: Online AP performance during indoor rotating hover scenario

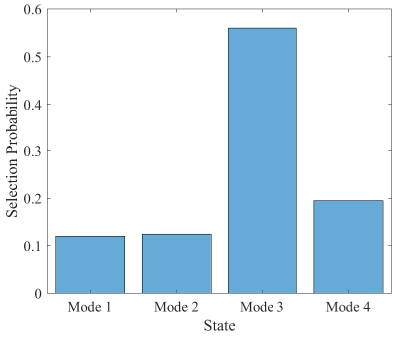

(A) Hover scenario

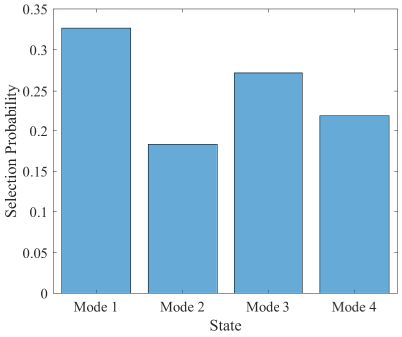

(B) Rotation hover scenario

FIGURE 8.3: Normalized mode selection histogram for hover and rotation hover scenarios

In the hover scenario the vehicle experienced minimal changes in heading so the mode that yielded the highest reward likely did not change throughout the duration of the flight. Figure 8.3a shows that State 3 was chosen over 50% of the time, and the other modes were selected at rates in the range of 10%-20%, suggesting that State 3 offered the highest expected reward so the AP policy selected this mode with a high probability.

In the rotating hover scenario, the vehicle experienced large changes in heading which likely caused the reward distribution at each antenna mode to vary significantly throughout the duration of the flight. Figure 8.3b shows that AP policy

did not constantly exploit the same antenna mode with high selection probability throughout the duration of the flight, because the algorithm would adapt its antenna mode selection distribution exploit to the new best antenna mode each time the vehicle was rotated.

8.3 NLOS and Interference Scenarios

The NLOS scenario test resulted in a 0.6 dB gain over omni-directional (Figure 8.2). The significant decrease in AP performance in the NLOS scenario as compared to the LOS scenarios is due to the lack of a dominant LOS multipath component, which further decreases the benefit of directionality.

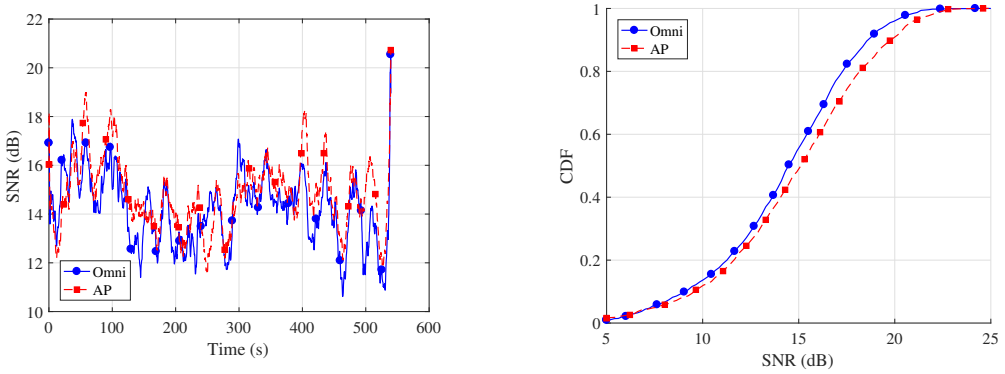

(A) Smoothed SNR measurements

(B) Online AP performance

FIGURE 8.4: Online AP performance during indoor NLOS scenario

The interference hover scenario results show AP provides a 1.4 dB mean SNR gain over omni-directional when co-channel interference is present (Figure 8.5). The performance increase AP provides in this scenario is likely greater than in the hover scenario. This increased performance can be attributed to the directional antenna patterns spatially filtering out the interfering signal since the interference source is located at a 90 degree offset from the transmitter. While the signal strength may be similar among the antenna modes due to multipath and scattering

in an indoor environment, there are likely to be antenna modes that exhibit better signal-to-interference ratio that the algorithm can exploit.

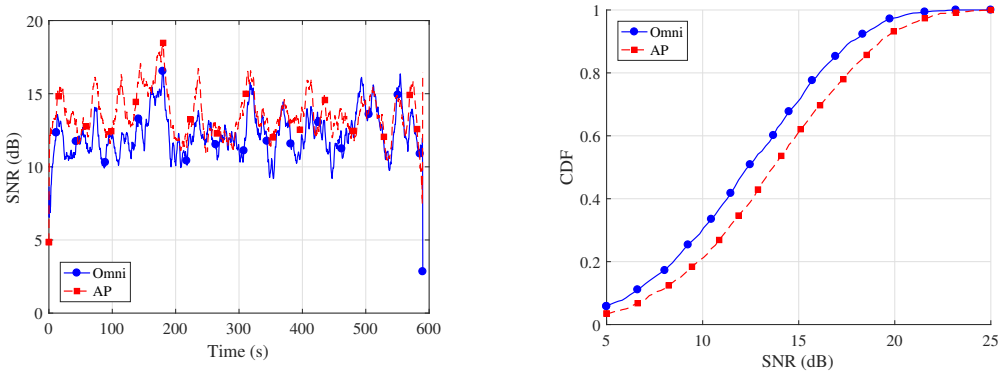

(A) Smoothed SNR measurements

(B) Online AP performance

FIGURE 8.5: Online AP performance during indoor interference scenario

8.4 Table of Results

It can now be concluded that that AP antenna selection strategy provides a mean SNR improvement over omni-directional antenna in high-multipath hover scenarios. The mean SNR gain of the adaptive beamsteering algorithm over the omni-directional antenna mode in each experiment is shown in Table 8.1. The gains are fairly modest in comparison to the outdoor experimental results presented in later chapters. Low SNR gains can be attributed to the rich scattering due to high multipath indoor environment, which lessens the advantages of directionality. It is important to note that for all experimental scenarios, there is no negative penalty for using the adaptive beamsteering approach over omni-directional, as the beamsteering algorithm does not increase the probability of receiving low SNR frames due to exploring relatively low performing antenna modes[1].

[1]This can be observed from the CDF comparisons, where the AP curve is always *to the right* of the omni-directional curve.

TABLE 8.1: Mean SNR gain of AP antenna selection strategy over omni-directional antenna mode

Scenario	**Mean SNR Gain over Omni (dB)**
Indoor Hover	1.23
Indoor Rotating Hover	1.1
Indoor NLOS Hover	0.6
Indoor Hover with Interference	1.4

9. Outdoor Flight Experiment

Chapter 8 shows that the adaptive beamsteering algorithm works in various conditions in an indoor environment. This chapter focuses on outdoor flight experiments that were conducted to compare the AP policy and omni-directional antenna mode performance in a more realistic environment.

9.1 Experimental Setup

A 10 minute flight was conducted outdoors on Drexel University's campus. The ground node was placed on a cart three ft. above the ground. The UAV was flown at an approximate horizontal distance of 42 ft. from the ground transmitter node, and an approximate height 22 ft. above the ground, which produces a elevation angle near 30 degrees. To account for the increased distance between the transmitter and receiver, a higher transmission power of 19 dBm was used. The flight was conducted in moderate weather with a slight breeze. Due to wind disturbances and the lack of GPS assisted flight, the UAV experienced larger position deviations than in the indoor flight. The vehicle heading was rotated 180 degrees in the middle of the flight.

9.2 Results

The AP policy produced a 2.06 dB SNR gain over omni-directional (Figure 9.4). The smoothed SNR measurements show significant SNR fluctuations of up to 10 dB caused by UAV movements (Figure 9.3). Although the outdoor flight experienced greater aerodynamic disturbances and changes in heading angle in comparison to indoor hover flights, the variance in omni-directional SNR was measured to be 11.7 dB, which is less than indoor flight variance of 16 dB.

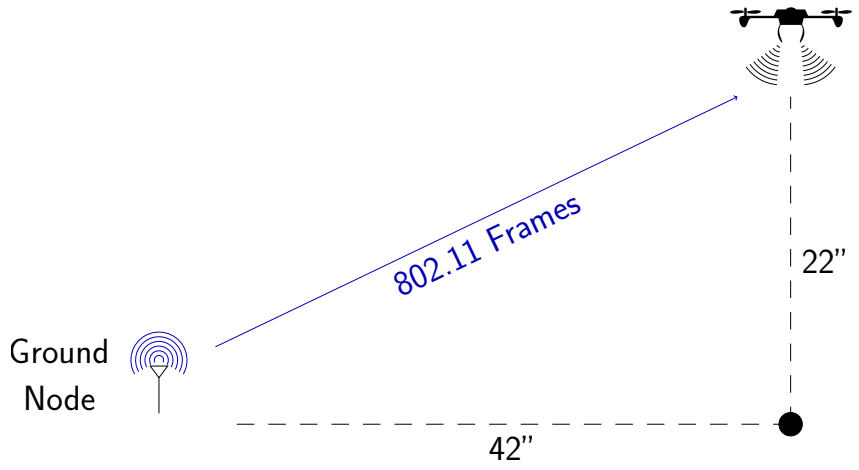

FIGURE 9.1: Outdoor flight topology showing relative positioning of the UAV and ground node

FIGURE 9.2: Outdoor flight with ground node located on the cart in the far right hand side of the image

There is a significant performance increase in the adaptive beamsteering algorithm in outdoor environments. This is expected because the indoor setting is a more challenging environment for exploiting directionality of wireless links compared to an outdoor environment which has less scattering and multipath

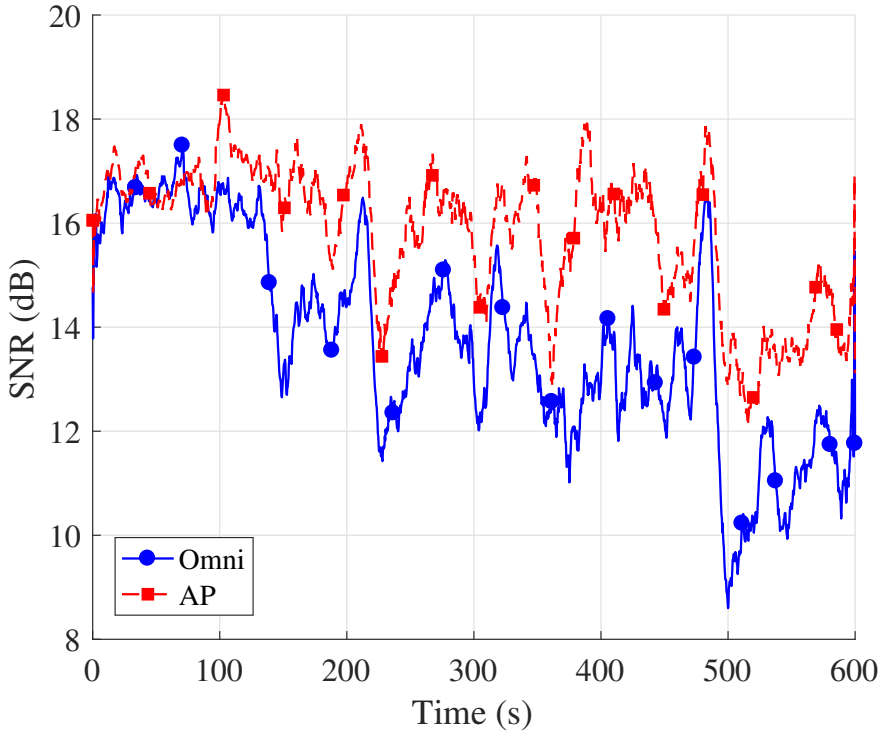

FIGURE 9.3: Smoothed SNR measurements from outdoor flight

effects. Unlike outdoor scenarios, where the LOS antenna orientation provides the highest signal strength and is generally the best antenna configuration, there could be multiple non-LOS antenna modes with comparable signal strength in indoor environments, making the antenna mode selection problem more difficult.

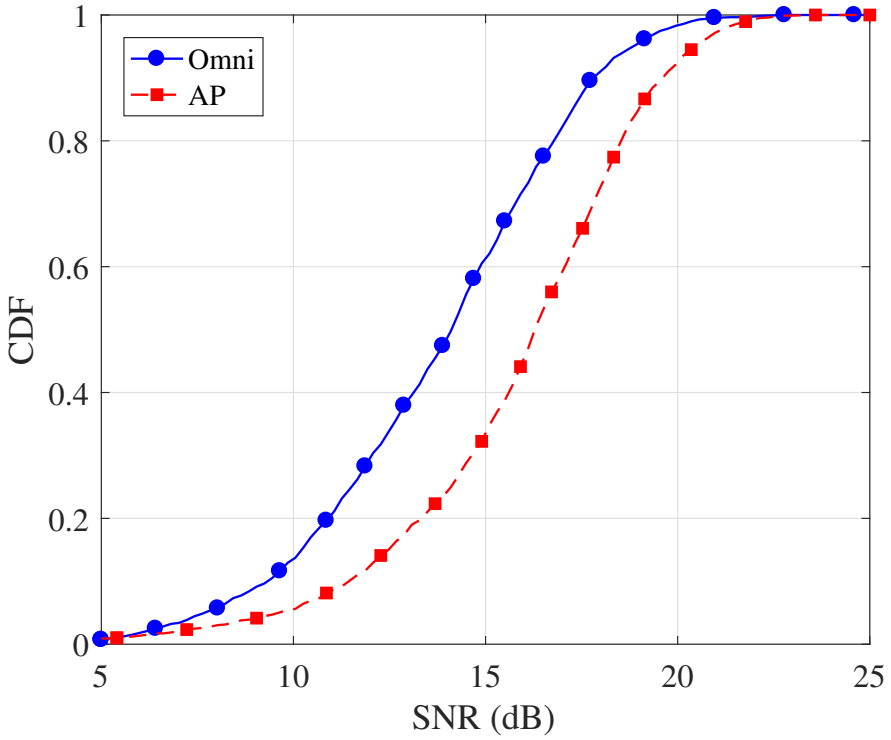

FIGURE 9.4: Online AP performance during outdoor flight

10. Reactive Jamming Mitigation Experiment

Unlike continuous jammers which transmit a continuous jamming signal on a specific frequency band, reactive jammers jam transmissions that are already *on-air* by transmit a short jamming burst when a radio transmission is detected. Reactive jammers are more power efficient and are harder to detect than traditional jammers, but are much more complex and difficult to implement. The capability of the adaptive beamsteering algorithm to avoid utilizing antenna modes the yield low SNR rewards is also capable of combating adversarial reactive jammers. This chapter presents experiments and results showing how our adaptive beamsteering algorithm is capable of mitigating reactive jammers by avoiding antenna modes that receive high jamming interference (Figure 10.1).

The reactive jammer described in [38] was utilized for these experiments. The reactive jammer used an energy detection technique to sense when the ground node started a frame transmission. When a transmission was detected, the reactive jammer would transmit a jamming burst with a duration of approximately 1 ms in hopes of jamming the ground node's transmitted frame.

10.1 Initial Testing

In order for the adaptive beamsteering algorithm to mitigate the reactive jammer, the AP reward metric needs to be negatively affected by the jammer. As shown in the indoor interference hover scenario, the previously used SNR-based reward works because it measures SINR when interference is present.

Typically 802.11 reactive jammers try to jam the frame's preamble in hopes of disrupting frequency offset estimation and channel estimation which likely leads

to decoding errors [39]. Therefore it makes sense to use the previously implemented SNR estimation method described in 5 which utilizes the 802.11 preamble to calculate SNR.

In order for the jammer to be able to jam the reception of the preamble, it needs to very quickly detect transmissions and respond with a jamming signal within 20 microseconds. An initial test was performed to check to see if the jamming signal arrived at the vehicle's onboard SDR receiver before the LTS portion of the preamble. This is necessary information, because if reactive jammer was unable to detect the ground node's transmission and start the jamming burst before the UAV's radio received the LTS symbols, the jamming signal will arrive at the receiver during the data portion of the frame. Since the implemented SNR estimation method utilized only the LTS portion of the 802.11 preamble, the

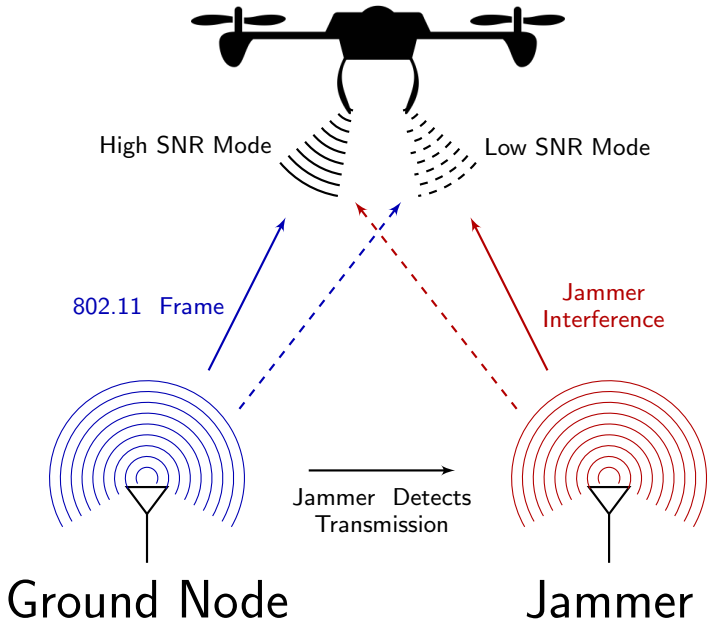

FIGURE 10.1: Reactive jamming mitigation concept diagram

delayed jamming signal will not be detected[1].

The UAV was placed in a stationary non-flight position, and the ground node transmitted frames in a manner similar to previous experiments at a transmit power of 19 dBm. The UAV would measure SNR from received frames in a manner similar to previous experiments, except that only the omni-directional antenna mode was utilized. The reactive jammer, which was transmitting 1.3 dBm jamming bursts, was turned on and off several times in 30 second increments. The results show that the average measured SNR decreased by 10 dBm when the jammer was on (Figure 10.2). Since SNR is the reward that the AP policy receives and is negatively affected by the jammer, the algorithm should be able to choose the best antenna states to mitigate the reactive jammer.

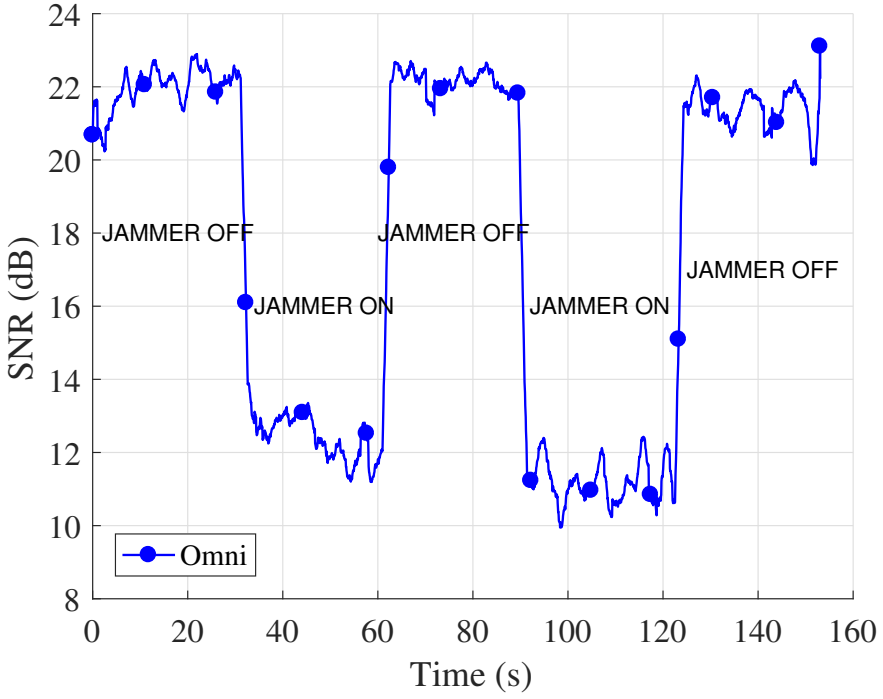

FIGURE 10.2: Smoothed SNR measurements from the omni-directional antenna state in a non-flight setting with the reactive jammer toggled on and off in 30 second increments

[1]If the jamming signal arrived after the preamble, a different SNR estimator could be implemented such as the average EVM squared method described in [37].

10.2 Outdoor Experimental Setup

Outdoor flights were conducted on Drexel University's campus in the presence of an adversarial reactive jammer in a realistic environment. The reactive-jammer would detect transmissions from the ground node and immediately transmit a high power jamming signal which would reduce the SNR measured at the receiver (Figure 10.4). The UAV hovered approximately 18 ft. above the ground. The ground transmitter node was placed on a cart 3 ft. above the ground at a horizontal distance of approximately 35 ft. from the UAV. The jamming antenna was positioned on a cart approximately 37 ft. away from the UAV, 4 ft. above the ground (Figure 10.3). The jammer used the same omni-directional antenna as the ground node.

Two flights were conducted with varying jamming powers. The first experiment was a 9 minute flight where the ground node transmission power was 19 dBm and the jammer power was 1.3 dBm. The second experiment was a 10 minute flight where the ground node transmitter power remained the same, but the jammer transmitter power was reduced to -8.3 dBm.

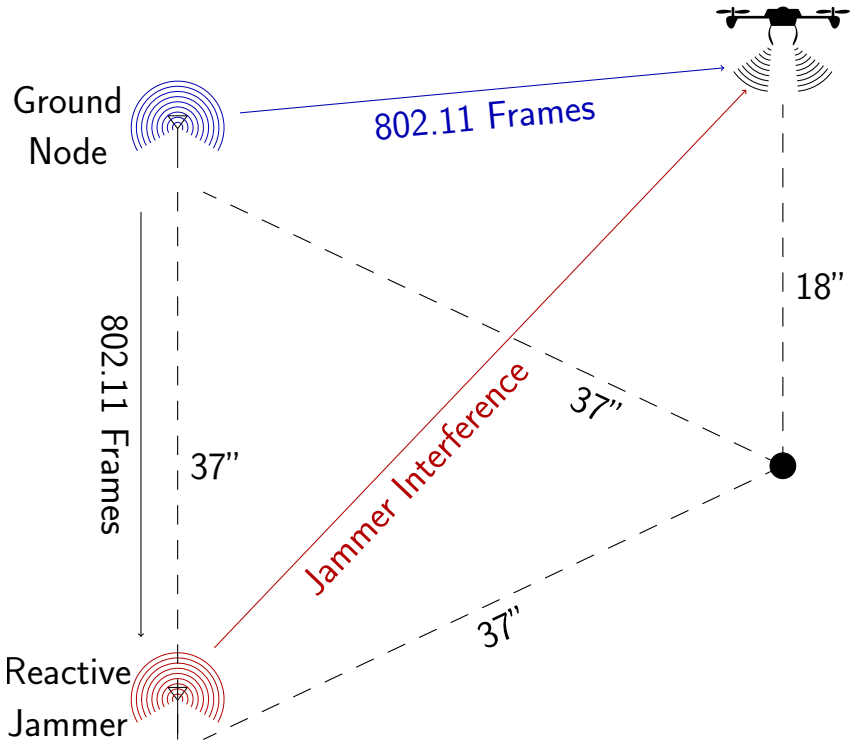

FIGURE 10.3: Reactive jamming experiment topology showing the relative positioning of the UAV, ground position, and reactive jammer

FIGURE 10.4: Experimental flight with reactive jammer (leftmost cart), ground node (rightmost cart) and UAV in the air on the right-hand side of the image

10.3 Results

The first flight was conducted in the presence of an adversarial reactive jammer with a transmission power of 1.3 dBm (Figure 10.5). The AP policy produced a 2.4 dB gain over omni-directional.

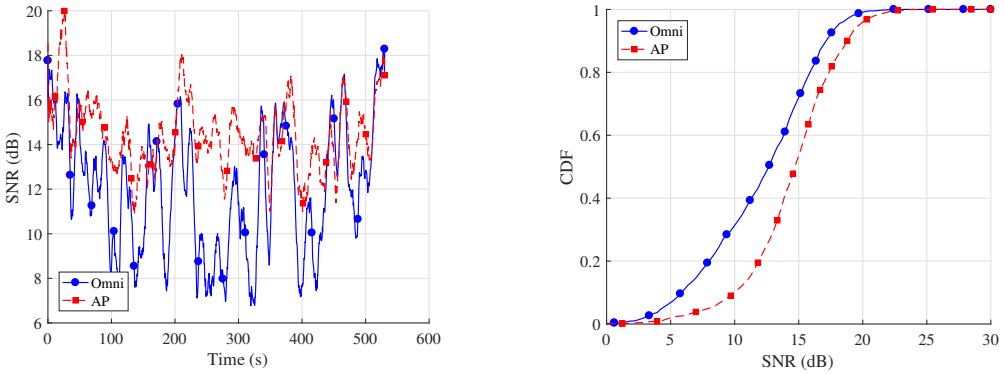

(A) Smoothed SNR measurements (B) Online AP performance

FIGURE 10.5: Online AP performance with high-power adversarial reactive jammer

The second flight was conducted in a similar manner as the first flight, and the jammer with a transmission power was reduced by 10 dB to -8.3 dBm (Figure 10.6). The AP policy produced only a 1.0 dB gain over omni-directional. The reduced AP performance may be partially attributed to the fact that the second flight was conducted under slightly different wind conditions.

The results show that the AP beamsteering strategy can be used to help combat adversarial reactive jammers by providing increased SNR. It is important to note that the results from the second anti-jamming flight showed that adaptive beamsteering strategy offered significantly less mean SNR gain than the second.

The theory for this difference in performance is likely due to the fact that the 90-degree antenna azimuth angle is larger than the angle between the reactive jammer and ground node. This creates a topology where some UAV heading angles

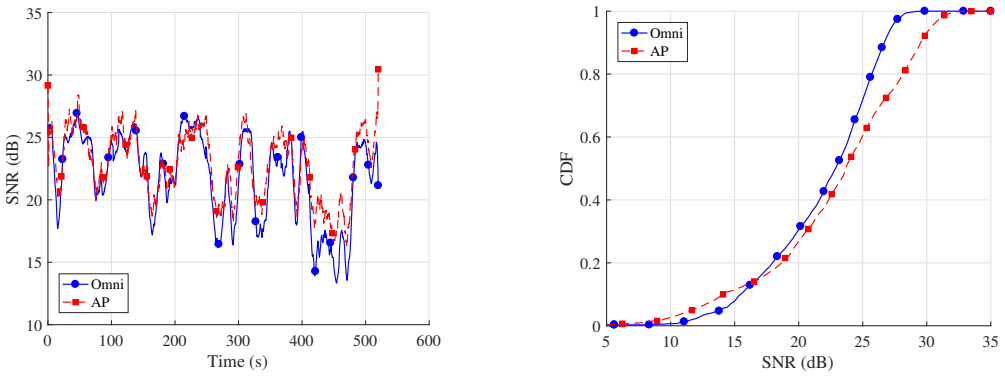

(A) Smoothed SNR measurements (B) Online AP performance

FIGURE 10.6: Online AP performance with low-power adversarial reactive jammer

orient the antenna such that the modes that receive the maximum signal and interference power are different causing high jammer mitigation performance, and some UAV heading angles where the received maximum signal and interference power occur at the same antenna mode which leads to low jammer mitigation performance (Figure 10.7). Since the heading angle could vary up to 30 degrees due to the lack of an onboard compass, we believe that deviations in heading angle

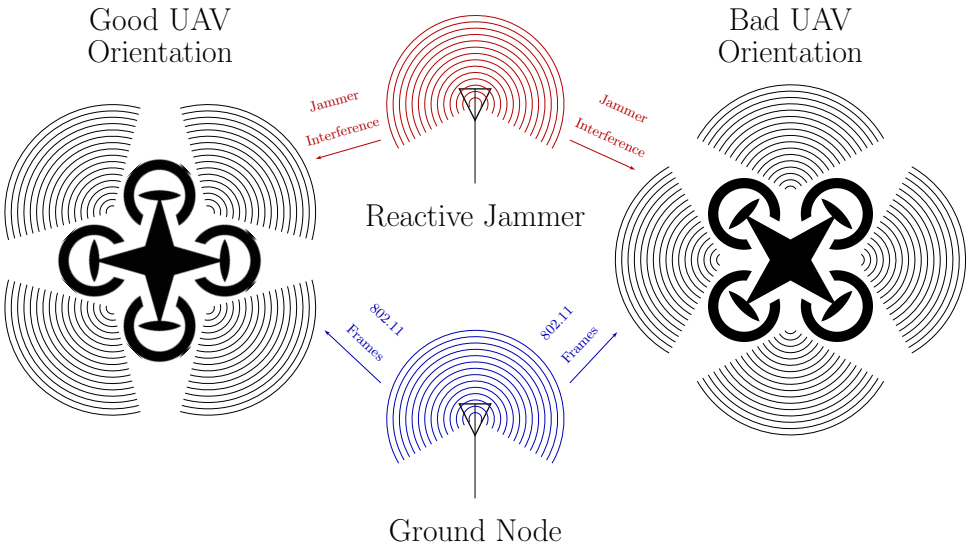

FIGURE 10.7: Illustration of how heading angle may affect reactive jamming mitigation performance in small-angle scenarios

partially contribute to these performance differences between flights.

Further experimentation is necessary at various angles between the ground node and jammer to develop a better understanding of how reactive jamming mitigation performance is affected by the topology. However, these preliminary results show that the beamsteering algorithm is still capable of providing a mean SNR gain with various jammer power with a 60 degree angle between the ground node and jammer.

The results from all adaptive beamsteering scenarios are shown in Table 10.1.

TABLE 10.1: Mean SNR gain of AP antenna selection strategy over omni-directional antenna mode

Scenario	**Mean SNR Gain Over Omni (dB)**
Outdoor Flight	2.06
Outdoor with Reactive Jammer (1.3 dBm)	2.4
Outdoor with Reactive Jammer (-8.4 dBm)	1.0
Indoor Hover	1.23
Indoor Rotating Hover	1.1
Indoor NLOS Hover	0.6
Indoor Hover with Interference	1.4

11. Conclusion and Future Work

11.1 Conclusion

This thesis shows a system design for an aerial wireless research platform built around a hexacopter airframe. The system has a highly reconfigurable radio system payload that includes an B200-mini SDR and an electrically reconfigurable antenna. The wireless payload is capable of running various GNU Radio projects. The design is the first multicopter-based aerial testbed with a highly configurable SDR system designed for generic research purposes.

The aerial wireless research platform was used to implement adaptive beamsteering algorithms utilizing the reconfigurable antenna. The SNR distribution at each utilized mode of the reconfigurable antenna in both non-airborne and airborne flight. The results show that there is nearly always at least one directional state that would produce a higher SNR than the omni-directional mode in a given topology. If the radio was able to learn and utilizes the states with high SNR, it could improve average SNR. The measured SNR gain that reconfigurable directional antenna and selection algorithms provides over omni-directional antenna and show that reconfigurable antennas and selection algorithms can be used to increase mean SNR by approximately 2 dB for wireless links between UAVs and ground nodes without any negative penalties due by antenna mode exploration. We also show that adaptive pursuit is still capable of outperforming an omni-directional antenna in more severe scenarios, such as indoor NLOS environments where the benefit of directionality is minimal. Lastly, this thesis presents experimental results that show that the implemented beamsteering algorithm can also be used to combat an adversarial reactive jammer by selecting avoiding antenna

states that yield low SINR rewards. The results of all flight experiments are shown in Table 10.1.

Experimental results shown in this thesis are the first measurements which utilize reconfigurable antennas or adaptive beamsteering algorithms on a multi-copter UAV.

11.2 Future Work

Embedded SDR radios are relatively new and expensive, and SDR frameworks such as GNU Radio are computationally intensive. Embedded single-board computers such as the Raspberry Pi 3 are just starting to become powerful enough to run SDR applications. In the future, more powerful embedded computers will exist at cheaper prices and smaller form-factors. Currently, only 1 in 30 frames are used as rewards by the AP policy. In the future, we plan to utilize more powerful onboard computers which will allow the AP policy to acquire rewards at a faster rate.

The results show that continuous movement of the UAVs antenna reduces the performance of the adaptive beamsteering algorithm. Wind and other aerial disturbances cause significant deviations in the vehicle's position and attitude which likely increases the severity of this motion, and therefore the performance of the adaptive beamsteering algorithm. The outdoor experiments did not have the ability to measure these aerial disturbances and characterize their effect on the air-to-ground link. Future work should analyze how wind and weather affects the performance of the adaptive beamsteering algorithm.

As described in Chapter 6.1.2, work may also involve fusing onboard UAV sensor data with the reinforcement learning-based beamsteering strategy for online

tuning of the exploration/exploitation rates.

Appendix A: List of Symbols

H	Channel State Information	(unitless)
K_v	Motor Constant	RPM V^{-1}
K	Rician K-factor	(unitless)
P	Power (UAV)	watts
P_{TX}	Transmit Power	watts/dBm
P_{RX}	Receive Power	watts/dBm
T	thrust	grams
T_d	Symbol Duration	s
F_T	Maximum Thrust	newtons
M_g	Gross Vehicle Weight	grams
$\mathcal{N}_c$	Circularly-Symmetric Complex Normal Distribution	(unitless)
N	Noise Power	watts/dBm
S	Signal Power	watts/dBm
X	Transmitted Constellation Point	(unitless)
Y	Received Constellation Point	(unitless)
y	Received Signal	(unitless)
W	Additive White Gaussian Noise	(unitless)
η	Efficiency	(unitless)
ν	LOS Signal Amplitude	(unitless)
σ	Multipath Signal Amplitude per I/Q Channel	(unitless)

Appendix B: System Weight and Power Budget

Table B.1: Total System Weight Budget

Weight Budget	
Component	Weight (g)
Airframe	478
LiPo Battery	552
Propellers (x6)	78
Motors (x6)	360
ESCs (x6)	258
MCU	27
PMU	28
LEDs	13
RC Receiver	25
Mounting and Cabling	100
Total UAV Weight	1919
Raspberry Pi 3	45
USRP B200-mini	24
DC-DC Converter	20
Antenna	20
Mounting and Cabling	150
Total Payload Weight	259
Gross Takeoff Weight	2128
Maximum Gross Takeoff Weight	2400

Table B.2: Total System Power Budget

Power Budget			
Component	Average Current Draw (A)	Nominal Supply Voltage (V)	Average Power (W)
ESCs & Motors (x6) (measured)	13	14.8	192.4
PMU, Naza, and LED [40]	0.12	5	0.6
RC Receiver [41]	0.10	5	0.5
Total UAV Power			193.5
Raspberry Pi 3 [42]	0.85	5	4.25
USRP B200-mini [30]	0.50	5	2.5
Alford Loop (measured)	0.10	5	0.5
Total SDR Power			7.25
Total System Power			201

Appendix C: FAA UAS Regulations

Throughout the duration of this project FAA regulations of Small UAS [1] have been in flux. When the project was first proposed in October 2015, no Small UAS regulations existed for non-commercial applications. The frequent changing in regulations, and their ambiguity toward Small UAS applications in academia made it difficult to determine the legality of flying the UAV in an outdoor environment.

C.1 FAA Small UAS Regulation Timeline

FAA Modernization and Reform Act of 2012 (FMRA), prohibited commercial operation of UAS in NAS. However, it was possible for commercial entities to petition for exemption under Section 333 of FMRA. The FAA would grant Section 333 Exemptions on a case-by-case basis [43]. Over 5,000 Section 333 Exemptions have been granted since FMRA took effect [44]. Hobbyist UAS operation was legal, however hobbyist operation rules were declared in FMRA Section 336 [45]. In December 21, 2015, the additional Small UAS regulations took effect on December 21, 2015. Hobbyist UAS weighing more than 0.55 lbs. are required to be registered by the FAA.

On August 29, 2016, Part 107 was added to the Title 14 Code of Federal Regulations (14 CFR). Part 107 is an additional set of rules intended allow Small UAS to be used for commercial purposes [46]. Part 107 operational rules are

[1] Terminology note: A UAV consists of only the vehicle and onboard components. FAA documentation refers *drone* operation as *UAS* (Unmanned Aerial System) operation. The term UAS refers to the UAV, controller on the ground, and communication links between the two. While *UAV* just refers to the aerial vehicle and onboard components.

typically similar to Section 336 hobbyist operation rules. However, operation under Part 107 requires that the remote pilot in command passes has a remote pilot certification. The certification requires that the remote pilot passes an FAA-approved aeronautical knowledge exam.

C.2 Current FAA Small Unmanned Aircraft Rules

Given the desired flight plan for low-altitude aerial wireless system research, the most relevant FAA Part 107 and Section 336 rules are as follows:

1. Ensure the aircraft complies with existing registration requirements.
2. Aircraft must remain in Visual line-of-sight (VLOS) of the remote pilot in command.
3. Aircraft cannot exceed a maximum altitude of 400 ft. AGL.
4. Operate only in the time between 30 minutes before official sunrise and 30 minutes after official sunset).
5. Operations in Class B, C, D, and E airspace require ATC permission.
    (a) Operations in Class G airspace do not require ATC permission.
6. UAS must yield right-of-way to other aircrafts
7. External load operations are allowed if the object being carried by the unmanned aircraft is securely attached and does not adversely affect the flight characteristics or controllability of the aircraft.

C.3 Airspace Classsification and Regions

Airspace that is part of NAS is split into five different classes: A, B, C, D, E, and G. Classes A through E are controlled airspace controlled by ATC (Figure C.1). Class G is uncontrolled airspace. Each airspace class has different restrictions and operating rules.[4].

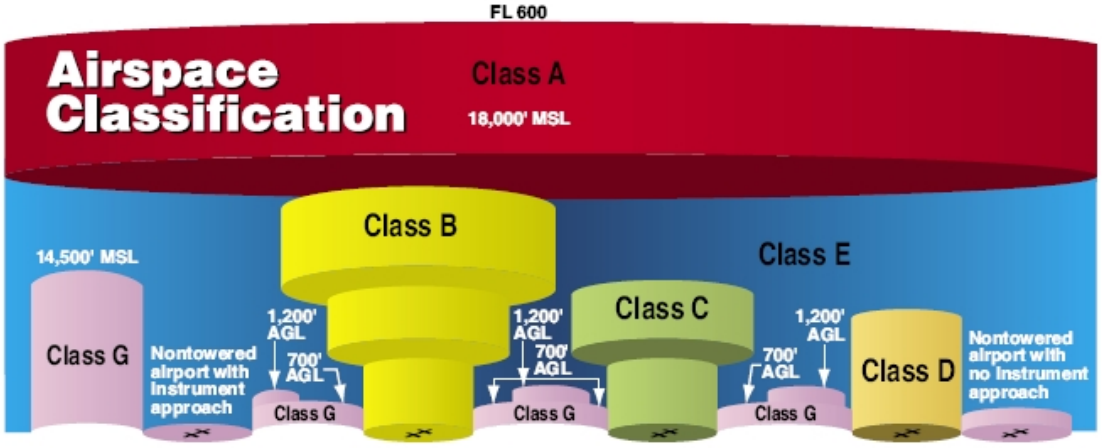

FIGURE C.1: Profiles of FAA Airspace Classes [4].

Class A consists of high-altitude airspace which is typically from 18,000 ft. above MSL to 60,000 ft. above MSL. Class A airspace is heavily restricted. Operations in Class A airspace require ATC clearance.

Class B airspace is heavily controlled high-traffic airspace surrounding busy airports. ATC clearance is required to enter Class B airspace. The shape of Class B airspace may vary from airport to airport, but it is typically shaped like an upside down cone which widens at higher altitudes. Class C and D airspace is airspace surrounding medium and small sized airports. Class C typically extends from surface to 4,000 ft. above airport elevation, and Class C typically extends from surface to 2,500 ft. above airport elevation. Like Class B airspace, Class B and D may be shaped like an upside down cone. Class E airspace is controlled

airspace that is not Class A, B, C, or D airspace. Class E airspace generally extends from 1,200 feet AGL to 18,000 ft. MSL.

Class G is uncontrolled airspace. Class G consists of all airspace that is not part of classes A through E. ATC permission is not required before UAV operation in Class G airspace [46].

C.3.1 Airspace Classification on Drexel University's Campus

FIGURE C.2: Sectional map of Class B airspace over Philadelphia. Drexel University's campus is marked in red [5].

Outdoor UAV flights would take place on Drexel University's Campus. The Philadelphia International Airport (PHL) is located approximately 6.5 miles south-south-west of Drexel University. Class B airspace surrounds PHL [5]. The sectional map of the Class B airspace over Philadelphia shows that Drexel University is in a

section marked with $\frac{70}{15}$ (Figure C.2). The $\frac{70}{15}$ notation represents the minimum and maximum height of the Class B region in hundreds of feet above MSL. Therefore, the above airspace has a Class B region ranging from 1,500 ft. above MSL to 7,000 ft. above MSL.

Below the Class B airspace floor of 1,500 ft. above MSL over Drexel University's campus, there is a Class E section extending from 700 ft. AGL to 1,500 ft. above MSL [5]. The airspace below 700 ft. AGL is uncontrolled Class C airspace. Considering UAVs are only permitted to operate below 400 ft. AGL (approximately 450 ft. MSL on Drexel University's campus), the UAV will not enter controlled airspace when operating within FAA regulations.

C.3.2 Mode C Veil

As of September 15, 2015, all Class B airports, including the Philadelphia International Airport, are surrounded by Mode C veil. The Mode C veil consists of all airspace within a 30 nautical mile horizontal radius from the airport, extending vertically from ground surface to 10,000 ft. above MSL [47]. The mode C does not specify airspace Class, however within the Mode C veil, most operational aircrafts are required to have a Mode C transponder. The Mode C veil is not an airspace class, nor does it affect on the airspace class within the veil.

Drexel University campus falls within the Mode C veil centered on the Philadelphia International Airport. However, aircrafts without a engine-driven electrical system are exempt from the Mode C veil's transponder rule [48]. Battery powered UAS do not have a engine-driven electrical system, therefore a Mode C transponder is not required.

C.4 Conducted UAS Operations

Indoor airspace is not considered part of NAS and is not regulated by the FAA [49]. Therefore, it is legal to fly any aircraft indoors without vehicle adhering to FAA regulations and registration. Most experiments involving UAV flight were conducted indoors both the 3rd floor atrium of Drexel University Bossone Research Center and in Drexel MESS Lab. The UAV was registered under section 336 for recreational flight, and flown outdoors over a grass area on Drexel University's campus near 3200 Market. During outdoor flight, the vehicle's altitude was never higher than 25 ft. MSL.

Bibliography

[1] How non-line-of-sight backhaul really works. [Online]. Available: https://www.wirelessdesignmag.com/blog/2012/09/how-non-line-sight-backhaul-really-works

[2] 802.11 OFDM overview. [Online]. Available: http://rfmw.em.keysight.com/wireless/helpfiles/89600b/webhelp/subsystems/wlan-ofdm/content/ofdm_80211-overview.htm

[3] D. Patron and K. R. Dandekar, "Planar reconfigurable antenna with integrated switching control circuitry," in *Antennas and Propagation (EuCAP), 2014 8th European Conference on*. IEEE, 2014, pp. 2737–2740.

[4] Pilot's handbook of aeronautical knowledge (FAA-H-8083-25B). chapter 15: Aerospace. [Online]. Available: https://www.faa.gov/regulations_policies/handbooks_manuals/aviation/phak/media/17_phak_ch15.pdf

[5] Digital aviation, llc. [Online]. Available: http://vfrmap.com/

[6] F. Jiang and A. L. Swindlehurst, "Optimization of UAV heading for the ground-to-air uplink," *IEEE Journal on Selected Areas in Communications*, vol. 30, no. 5, pp. 993–1005, June 2012.

[7] P. B. Charlesworth and S. M. Allen, "Use of dynamic flight paths to enhance support to priority subscribers on a communications UAV," in *MILCOM 2012 - 2012 IEEE Military Communications Conference*, Oct 2012, pp. 1–6.

[8] B. Galkin, J. Kibilda, and L. A. DaSilva, "Deployment of UAV-mounted access points according to spatial user locations in two-tier cellular networks," in *2016 Wireless Days (WD)*, March 2016, pp. 1–6.

[9] J. Romeu, A. Aguasca, J. Alonso, S. Blanch, and R. R. Martins, "Small UAV radiocommunication channel characterization," in *Proceedings of the Fourth European Conference on Antennas and Propagation*, April 2010, pp. 1–5.

[10] DJI. [Online]. Available: http://www.dji.com

[11] CyPhy Works, Inc. [Online]. Available: cyphyworks.com

[12] Y. Gu, M. Zhou, S. Fu, and Y. Wan, "Airborne WiFi networks through directional antennae: An experimental study," in *2015 IEEE Wireless Communications and Networking Conference (WCNC)*, March 2015, pp. 1314–1319.

[13] E. Yanmaz, R. Kuschnig, and C. Bettstetter, "Channel measurements over 802.11a-based UAV-to-ground links," in *2011 IEEE GLOBECOM Workshops (GC Wkshps)*, Dec 2011, pp. 1280–1284.

[14] O. Andryeyev, O. Artemenko, and A. Mitschele-Thiel, "Improving the system capacity using directional antennas with a fixed beam on small unmanned aerial vehicles," in *2015 European Conference on Networks and Communications (EuCNC)*, June 2015, pp. 139–143.

[15] T. J. Willink, C. C. Squires, G. W. K. Colman, and M. T. Muccio, "Measurement and characterization of low-altitude air-to-ground MIMO channels," *IEEE Transactions on Vehicular Technology*, vol. 65, no. 4, pp. 2637–2648, April 2016.

[16] C. M. Cheng, P. H. Hsiao, H. T. Kung, and D. Vlah, "Performance measurement of 802.11a wireless links from UAV to ground nodes with various antenna orientations," in *Proceedings of 15th International Conference on Computer Communications and Networks*, Oct 2006, pp. 303–308.

[17] GNU Radio. [Online]. Available: https://gnuradio.org/

[18] N. Gulati and K. R. Dandekar, "Learning state selection for reconfigurable antennas: A multi-armed bandit approach," *IEEE Transactions on Antennas and Propagation*, vol. 62, no. 3, pp. 1027–1038, March 2014.

[19] S. Begashaw, D. H. Nguyen, and K. R. Dandekar, "Enhancing blind interference alignment with reinforcement learning," in *2016 IEEE Global Communications Conference (GLOBECOM)*, Dec 2016, pp. 1–7.

[20] S. H. Kim, B. H. Jung, and D. K. Sung, "Adaptive beamforming antenna scheme to minimize the interference in a unmanned aerial vehicle (UAV) MANET," in *2009 IEEE 20th International Symposium on Personal, Indoor and Mobile Radio Communications*, Sept 2009, pp. 813–817.

[21] D. Thierens, "An adaptive pursuit strategy for allocating operator probabilities," in *Proceedings of the 7th Annual Conference on Genetic and Evolutionary Computation*, ser. GECCO '05. New York, NY, USA: ACM, 2005, pp. 1539–1546. [Online]. Available: http://doi.acm.org/10.1145/1068009.1068251

[22] B. Bloessl, M. Segata, C. Sommer, and F. Dressler, "An IEEE 802.11a/g/p OFDM receiver for GNU Radio," in *Proceedings of the Second Workshop on Software Radio Implementation Forum*, ser. SRIF '13. New York, NY, USA: ACM, 2013, pp. 9–16. [Online]. Available: http://doi.acm.org/10.1145/2491246.2491248

[23] non-x86 support: Only use SSE2 when supported. [Online]. Available: https://github.com/bastibl/gr-ieee802-11/pull/49

[24] S. Wolfe, S. Begashaw, Y. Liu, and K. R. Dandekar, "Adaptive link optimzation for 802.11 UAV uplink using a reconfigurable antenna," in *MILCOM*

2017 - 2017 IEEE Military Communications Conference, Oct Under Review, pp. 1–6.

[25] DJI lightbridge. [Online]. Available: http://www.dji.com/lightbridge-2

[26] Z. Wu, H. Kumar, and A. Davari, "Performance evaluation of OFDM transmission in uav wireless communication," in *Proceedings of the Thirty-Seventh Southeastern Symposium on System Theory, 2005. SSST '05.*, March 2005, pp. 6–10.

[27] M. Rice, R. Dye, and K. Welling, "Narrowband channel model for aeronautical telemetry," *IEEE Transactions on Aerospace and Electronic Systems*, vol. 36, no. 4, pp. 1371–1376, Oct 2000.

[28] Y. S. Meng and Y. H. Lee, "Measurements and characterizations of air-to-ground channel over sea surface at c-band with low airborne altitudes," *IEEE Transactions on Vehicular Technology*, vol. 60, no. 4, pp. 1943–1948, May 2011.

[29] Wireless LAN medium access control (MAC) and physical layer (PHY) specifications. [Online]. Available: https://pdos.csail.mit.edu/archive/decouto/papers/802.11a.pdf

[30] Ettus Research. [Online]. Available: https://www.ettus.com

[31] Embedded development with GNU radio. [Online]. Available: http://gnuradio.org/redmine/projects/gnuradio/wiki/Embedded

[32] Intel streaming SIMD extensions technology defined. [Online]. Available: http://www.intel.com/content/www/us/en/support/processors/000005779.html

[33] GNU radio digital TV source code. [Online]. Available: https://github.com/gnuradio/gnuradio/tree/master/gr-dtv/lib/dvbt

[34] D. Raymer, A. I. of Aeronautics, and Astronautics, *Aircraft design: a conceptual approach*, ser. Educ Series. American Institute of Aeronautics and Astronautics, 1989. [Online]. Available: https://books.google.com/books?id=F5tTAAAAMAAJ

[35] Thrust to weight ratio. [Online]. Available: https://www.grc.nasa.gov/www/k-12/airplane/fwrat.html

[36] J. A. Fernandez, D. D. Stancil, and F. Bai, "Dynamic channel equalization for IEEE 802.11p waveforms in the vehicle-to-vehicle channel," in *2010 48th Annual Allerton Conference on Communication, Control, and Computing (Allerton)*, Sept 2010, pp. 542–551.

[37] H. A. Mahmoud and H. Arslan, "Error vector magnitude to SNR conversion for nondata-aided receivers," *Trans. Wireless. Comm.*, vol. 8, no. 5, pp. 2694–2704, May 2009. [Online]. Available: http://dx.doi.org/10.1109/TWC.2009.080862

[38] D. Nguyen, C. Sahin, B. Shishkin, N. Kandasamy, and K. R. Dandekar, "A real-time and protocol-aware reactive jamming framework built on software-defined radios," in *Proceedings of the 2014 ACM Workshop on Software Radio Implementation Forum*, ser. SRIF '14. New York, NY, USA: ACM, 2014, pp. 15–22. [Online]. Available: http://doi.acm.org/10.1145/2627788.2627798

[39] H. Rahbari, M. Krunz, and L. Lazos, "Swift jamming attack on frequency offset estimation: The achilles' heel of OFDM systems," *IEEE Transactions on Mobile Computing*, vol. 15, no. 5, pp. 1264–1278, May 2016.

[40] Naza-v2 specifications. [Online]. Available: http://www.dji.com/naza-m-v2/spec

[41] FrSky 2.4GHz ACCST X8R manual. [Online]. Available: www.frsky-rc.com/download/down.php?id=102

[42] Raspberry pi 3. [Online]. Available: https://www.raspberrypi.org

[43] Public guidance for petitions for exemption filed under section 333. [Online]. Available: https://www.faa.gov/uas/beyond_the_basics/section_333/how_to_file_a_petition/media/section333_public_guidance.pdf

[44] Authorizations granted via section 333 exemptions. [Online]. Available: https://www.faa.gov/uas/beyond_the_basics/section_333/333_authorizations

[45] Interpretation of the special rule for model aircraft. [Online]. Available: https://www.faa.gov/uas/media/model_aircraft_spec_rule.pdf

[46] Operation and certification of small unmanned aircraft systems. [Online]. Available: https://www.federalregister.gov/documents/2016/06/28/2016-15079/operation-and-certification-of-small-unmanned-aircraft-systems

[47] ATC transponder and altitude reporting equipment and use. [Online]. Available: https://www.gpo.gov/fdsys/pkg/CFR-2016-title14-vol2/xml/CFR-2016-title14-vol2-sec91-215.xml

[48] Unmanned aircraft operations in the national airspace system (NAS). [Online]. Available: https://www.gpo.gov/fdsys/pkg/CFR-2016-title14-vol2/xml/CFR-2016-title14-vol2-sec91-215.xml

[49] Federal aviation administration. [Online]. Available: www.faa.gov/uas/faqs/